Mon. Not. R. Astron. Soc. **000**, 1–?? (2014) Printed 16 April 2018 (MN LATEX style file v2.2)

A spinning supermassive black hole binary model consistent with VLBI observations of the S5 1928+738 jet

E. Kun[1,2⋆], K. É. Gabányi[1,3], M. Karouzos[4], S. Britzen[5], L. Á. Gergely[1,2,6]
[1] *Department of Experimental Physics, University of Szeged, Dóm tér 9, H-6720 Szeged, Hungary*
[2] *Department of Theoretical Physics, University of Szeged, Tisza Lajos krt 84-86, H-6720 Szeged, Hungary*
[3] *Konkoly Observatory, MTA Research Centre for Astronomy and Earth Sciences, P.O. Box 67, H-1525 Budapest, Hungary*
[4] *CEOU - Astronomy Program, Department of Physics & Astronomy, Seoul National University, Gwanak-gu, 151-742, Seoul, Korea*
[5] *Max-Planck-Institute für Radioastronomie, Auf dem Hügel 69, D-53121 Bonn, Germany*
[6] *Department of Physics, Faculty of Science, Tokyo University of Science, 1-3, Kagurazaka, Shinjuku, Tokyo 162-8601, Japan*

Accepted . Received ; in original form

ABSTRACT

Very Long Baseline Interferometry (VLBI) allows for high-resolution and high-sensitivity observations of relativistic jets, that can reveal periodicities of several years in their structure. We perform an analysis of long-term VLBI data of the quasar S5 1928+738 in terms of a geometric model of a helical structure projected onto the plane of the sky. We monitor the direction of the jet axis through its inclination and position angles. We decompose the variation of the inclination of the inner 2 milliarcseconds of the jet of S5 1928+738 into a periodic term with amplitude of $\sim 0.89°$ and a linear decreasing trend with rate of $\sim 0.05°\mathrm{yr}^{-1}$. We also decompose the variation of the position angle into a periodic term with amplitude of $\sim 3.39°$ and a linear increasing trend with rate of $\sim 0.24°\mathrm{yr}^{-1}$. We interpret the periodic components as arising from the orbital motion of a binary black hole inspiraling at the jet base and derive corrected values of the mass ratio and separation from the accumulated 18 years of VLBI data. Then we identify the linear trends in the variations as due to the slow reorientation of the spin of the jet emitter black hole induced by the spin-orbit precession and we determine the precession period $T_{\mathrm{SO}} = 4852 \pm 646$ yr of the more massive black hole, acting as the jet emitter. Our study provides indications, for the first time from VLBI jet kinematics, for the spinning nature of the jet-emitting black hole.

Key words: Galaxies: active – Quasars: supermassive black holes – Quasars: Individual: S5 1928+738

1 INTRODUCTION

The existence of Supermassive Black Holes (SMBH) at the centre of galaxies, combined with the important role of galaxy mergers in the hierarchical galaxy formation models and the long time-scale of the SMBH merging process suggest that SMBHs often exist in pairs (Blandford 1986; Searle & Zinn 1978; Komossa 2006). The binary passes through three evolutionary stages during the galaxy merger (Begelman et al. 1980). At first the stellar halo of each galaxy interacts with the central black hole of the other galaxy via dynamical friction (see e.g. Binney & Tremaine 1987). Gradually the black holes sink into a common gravitational potential well, and a bound, widely separated SMBH binary forms (a detailed review of massive black hole binary evolution can be found in Merritt & Milosavljević 2005). After this, a transition stage follows. The separation then decreases due to dynamical friction and beyond a transition radius the dissipation of energy and angular momentum becomes dominated by gravitational radiation. General relativistic effects during this inspiral stage are described in a post-Newtonian (PN) framework by expanding the field equations in terms of the PN parameter $\varepsilon = Gmc^{-2}r^{-1}$ (where m is the total mass, r is the separation, G is the gravitational constant, and c is the speed of light). PN techniques are involved in the description of merging binary-dynamics if $0.001 < \varepsilon < 0.1$, while in the plunge and the ring-down stages numerical calculations are required to characterize the final SMBH. The spins of the black holes generate corrections to the dynamics at 1.5PN orders through the spin-orbit coupling, at 2PN through the spin-spin coupling and at even higher orders through various post-Newtonian corrections to these couplings. The complicated PN dynamics in the presence of the spins is described in detail in e.g.

⋆ E-mail: kun@titan.physx.u-szeged.hu

Barker & O'Connell (1975, 1979), Kidder (1995), Gergely (2010a,b). When the spin and orbital momentum vectors are not aligned, a spin-orbit type precession will cause the spin vectors to slowly rotate about the orbital angular momentum vector.

SMBHs are believed to be the main engine of the activity in Active Galactic Nuclei (AGN) (for a review see e.g. Begelman et al. 1984). Apart from efforts of identifying binary black hole candidates in kpc-scale separated binaries with spatially resolved AGN (e.g. Komossa et al. 2003), indirect approaches have been also employed for the cases when gravitational radiation already dominates the merger of a sub-pc-scale separated binary. It has been estimated from the jet power, that at least one merger with orbital period of the order of one year should be detected in future blind surveys (at a nominal sky coverage of 10^4 deg^2 with 0.5 mJy sensitivity) through the electromagnetic (EM) signature of the SMBH binary on the jet (O'Shaughnessy et al. 2011), manifesting itself as an increase in the jet power when the binary inspirals toward its barycentre.

Relativistic bulk motion in the jet of AGN causes Doppler boosting of the synchrotron radiation of the relativistic particles. Very Long Baseline Interferometry (VLBI) observations reveal superluminally outward moving objects in a number of relativistic jets. Such superluminal motions are only apparent, indicating projection effects. These sources often show extreme variability throughout the EM spectrum. The radio variability can be explained in terms of flaring events following the ejection of jet-components or of a wiggling jet, implying a variable Doppler factor. AGN variability is however mostly non-periodic, hence detecting periodic behaviour of the radio light curve and precessing jets would strongly indicate a SMBH binary at the jet base (e.g. OJ287, Villata et al. 1998). While a plausible explanation for the precession of the jet is the existence of a merging SMBH binary at its base, alternative models allowing for a single black hole and external causes for the jet precession have been proposed (e.g. see the Discussion in Britzen et al. 2010, and references therein).

The precession of a jet originating in a SMBH binary system was discussed in e.g. Roos et al. (1993); Romero et al. (2000); Britzen et al. (2001); Lobanov & Roland (2005); Valtonen & Wiik (2012); Caproni et al. (2013). Several models have been developed to investigate the interaction between a SMBH binary and its astrophysical environment, revealing the presence of the binary in the AGN (e.g. MacFadyen & Milosavljević 2008; Tanaka & Haiman 2013). Recently, the helical modulation of the large-scale radio jet of J1502+1115 was attributed to the effect of the tight pair in a triple supermassive black hole system (Deane et al. 2014). Observational data have already been employed to identify precessing jet candidates. AGN observables allowed placing constraints on some of the SMBH binary parameters, like the total mass, the orbital period and the separation of the binary, e.g. Mrk 501, Villata & Raiteri (1999); 3C 273, Romero et al. (2000); BL Lac, Stirling et al. (2003); 3C 120, Caproni & Abraham (2004); 3C 345, Lobanov & Roland (2005); S5 1803+784, Roland et al. (2008); NGC 4151, Bon et al. (2012). The effect of the spin was not included in the calculations of these works, and the binary motion was approximated by pure Keplerian orbits.

The extreme Kerr-limit of the rotating SMBH is characterized by the value 1 of the dimensionless spin parameter χ (the spin S can be calculated as $S = Gc^{-1}m^2\chi$). However, as the accretion disk radiates and some of that radiation is trapped by the black hole, the extreme limit is actually not reached and rather the so-called canonical spin limit of $\chi_{\rm can} \simeq 0.998$ applies (Thorne 1974). A closed magnetic field line topology further connects the black hole horizon to the accretion disk, field lines acting as anchor chains, which further reduces the spin to $\chi \simeq 0.89$ (Kovács et al. 2011). Nevertheless this value is still extremely high, and as the presence of the jet signals a rich black hole environment, supporting the assumption of accretion, it is plausible to assume that at least the jet emitter black hole spins fast, and as such, the spin effects in the binary dynamics are non-negligible. The spin-powered jets are believed to be aligned with the black hole spin axis (Blandford & Znajek 1977), therefore precessing jets can reveal the presence of the spin.

In this paper we investigate the source S5 1928+738. This is a core-dominated quasar at a redshift $z = 0.302$, its luminosity distance is $D_{\rm L} = 1620$ Mpc, and at this distance the spatial resolution is 4.6 pc/milliarcsecond (where the cosmological parameters are $\Omega_{\rm m} = 0.314$, $\Omega_\lambda = 0.686$, $H_0 = 67.4$ km s^{-1} Mpc^{-1}, Planck Collaboration et al. 2013). The source is a well studied member of a complete sample of the extragalactic flat spectrum radio sources taken from the S5 strong source survey (Kühr et al. 1981). The VLA map at a wavelength of 20 cm (Johnston et al. 1987) reveals a structure comprising two lobes and a bright radio-core. Zooming into the jet base a one-sided core-jet structure appears on the milliarcsecond (mas) scale. The maximal apparent velocity detected in the jet, $8.1c$ (Lister et al. 2013) suggests high-speed bulk motion that is nearly head on, the mean jet direction is pointing close to the observer line of sight (LOS). This feature makes the jet a strongly Doppler-boosted one.

An analysis of the arcsecond- and the mas-scale jet structure has been published by Hummel et al. (1992) and the jet structure has been found to exhibit wiggles on both scales. A moving sine wave was fitted to the temporal motion of the components in the jet. Roos et al. (1993) proposed that the host galaxy of S5 1928+738 harbours a binary SMBH at its centre, inducing the periodic structures detected in the jet. A total mass of 10^8 M$_\odot$ was adopted, which would account for the bolometric luminosity on the basis of the Eddington limit. The orbital period was calculated to be ~ 2.9 years, the orbital separation ~ 0.005 pc and the mass ratio > 0.1. It has also been noted that if the wiggles in the mas-scale jet of S5 1928+738 are due to the orbital motion of a massive binary, the mean direction of the jet should obey a Lense-Thirring precession (Lense & Thirring 1918) about the orbital angular momentum of the binary, with a period of the order of 10^3 yr. Murphy & Edwards (2009) used the VLBI Space Observatory Programme data to further constrain the binary parameters by fitting their equations to jet component data from 8 epochs of observation performed at 5 GHz. The derived parameters are however affected by their assumption of the jet being emitted by the fictitious reduced mass particle.

The data collected on S5 1928+738 within the framework of the Monitoring Of Jets in Active galactic nuclei with VLBA Experiments (MOJAVE) survey span almost twenty years (Lister et al. 2009). Careful analysis of this dataset al-

lows us to detect and quantitatively analyse for the first time the spin-orbit precession of the jet emitter SMBH, manifesting itself as a small change over time in the direction of the jet axis. The spatial-length of the jet based on the MOJAVE-VLBI maps at 15 GHz and assuming an inclination of 7° is approximately 560 pc.

The paper is organised as follows. In Section 2 we summarize the observational techniques which can reveal periodicities in the extragalactic jets observed at radio wavelengths. More specifically we present methods based on the investigation of the AGN jet morphology, AGN jet kinematics and AGN jet flux density variability. In Section 3 we present the analysis of the archival MOJAVE data of S5 1928+738, investigating the temporal evolution of the jet structure. In Section 4, we describe a geometrical model for the three-dimensional (3D) helical jet structure. By projecting the spatial jet onto the plane of the sky and employing the maximal apparent velocity seen in the jet (which provides information about the inclination angle), we constrain the model by fitting it to the MOJAVE observations on the jet. Based on the jet modelling and on the independent total mass estimate, we give the binary parameters in Section 5. In Section 6 we discuss our findings and give our conclusions.

2 IDENTIFYING JET PRECESSION THROUGH OBSERVATIONS

Three main techniques have been employed to identify and study AGN jet precession.

2.1 AGN jet morphology

VLBI observations offer unparalleled spatial resolution and flux sensitivity compared to other wavelength regimes. VLBI studies thus allow the detailed investigation of the morphology of AGN jets and the inference of both physical and geometrical properties.

AGN jets have been known to exhibit strong curvature along their length and at all scales ranging from sub-pc to Mpc, although curvature appears to increase closer to the VLBI core (e.g. Krichbaum et al. 1994, 1995; Alberdi et al. 1997; Walker et al. 2001; Caproni & Abraham 2004; Savolainen et al. 2006). The curvature is usually identified in terms of the apparent position of individual jet components (e.g. Britzen et al. 2008), but also in terms of the jet as a whole. This is accomplished by the definition of the jet ridge line, a line that connects the centres of all VLBI jet components identified at a single epoch of observations (e.g. Hummel et al. 1992; Britzen et al. 2010; Karouzos et al. 2012b). The jet ridge line of AGN jets can be used to identify jets with strong variations of their curvature along the jet axis. Karouzos et al. (2012a), using a simple geometrical model of a helical jet, showed that a helically structured or a precessing jet can give rise to the curvature observed in many AGN jets.

2.2 AGN jet kinematics

VLBI observations at different epochs can reveal not only the overall shape of the jet but also the position and proper motion of the individual components that make up the jet. This proper motion is characteristic of both the physics of the components themselves (e.g. Marscher & Gear 1985) and the properties of the underlying jet, namely the presence of precession at the foot-point of the jet. In particular, non-ballistic motions, i.e., acceleration along the components' trajectories and/or significant non-radial motions can reveal the presence of a precessing jet. It has been shown that many AGN jet components follow helical trajectories which can be explained by means of plasma instabilities (e.g. Kelvin-Helmholtz instability, Camenzind & Krockenberger 1992; Hardee & Stone 1997; Perucho et al. 2006).

Several well-studied AGN have been found to show non-ballistic motions in their jets, which are interpreted in terms of a helical or precessing jet (e.g. Steffen et al. 1995; Abraham 1999; Britzen et al. 2009; Liu et al. 2010; Kudryavtseva et al. 2011a; Karouzos et al. 2012a).

The projected positions of individual components on the plane of the sky can be directly used for fitting of analytical models and can therefore usually constrain both the opening angle of the precession cone, the initial time and angle of ejection of each jet component, and given enough data, the periodicity of the jet precession and consequently of the binary black hole system. As described in the previous section, the sensitivity of the VLBI observations together with the density of the temporal sampling determine how accurately the precession properties can be derived. In addition, the study of individual jet component kinematics entails the cross-identification of components across epochs.

2.3 Flux density variability

Long-term monitoring of a source in the optical and/or radio allows the construction of a light curve that can be analysed in terms of jet precession and the presence of a BBH system. Given the relativistic speed in AGN jets, small variations in the angle between the trajectory of a jet component and our line of sight (LOS) can lead to significant flux variations due to the Doppler effect. Such angle changes are predicted in a precessing jet. In addition, for a precessing jet (unlike, e.g. for an expanding shock wave within the AGN jet) flaring events at different wavelengths are expected to be synchronous rather than lagging (e.g. Pyatunina et al. 2007; Kudryavtseva et al. 2011b). By analysing periodicities in AGN light curves (e.g. Fan et al. 2007; Kudryavtseva et al. 2011a) and more importantly by analysing the cross-correlation between light curves at different wavelengths (e.g. Quirrenbach et al. 1991; Britzen et al. 2009), one can deduce the periodicity of a possible precession. This methodology has been used to derive the parameters of a BBH system in OJ 287 (Villata et al. 1998), and in 3C 454.3 (Qian et al. 2007).

The difficulty of such flux variability studies lies in the dense sampling of the light curve that is required to robustly extract periodicity time-scales. In addition, the time-scales usually predicted by models of jet precession and BBH systems are of the order of several years (e.g. Roland et al. 1994; Steffen 1997; Caproni & Abraham 2004), implying that a source must be monitored for at least a similar (or longer) time period.

For the few sources for which both kinematic and photometric information is available, a combination of the above

three methods can constrain any precession or binary black hole model further. Notable examples include S5 1803+784 (Roland et al. 2008), PKS 0420-014 (Britzen et al. 2001), and 3C 345 (Lobanov & Roland 2005). In the next section we present the radio analysis of the mas-scale jet of S5 1928+738.

3 ANALYSIS OF ARCHIVAL MOJAVE DATA

3.1 Archival VLBA data

Observations of S5 1928+738 used in the present work were taken between 1994.67 and 2013.06 in 45 epochs with the Very Long Baseline Array (VLBA) at 15 GHz within the framework of the MOJAVE survey. The VLBA comprises ten radio telescopes, each with a diameter of 25 m. The longest baseline corresponds to 8611 km and the maximal number of possible baselines is 45. The half-power beam width is 0.47 mas at 2 cm (15.36 GHz). For more details of the observational setups see Lister et al. (2013) and references therein. We downloaded the 45 epochs of calibrated visibilities of S5 1928+738 from the MOJAVE webpage[1] and model-fitted them using the Caltech DIFMAP software package (Shepherd 1997). The image parameters and main results concerning our model-fits are summarized in Table 1. During the model-fitting process circular or elliptical Gaussian components are used to parametrize the brightness distribution of the jet and model the jet as the sum of a number of 2-dimensional Gaussian components. Performing model-fitting on data of several years one can trace the temporal change in the properties of the components; any change reflects the evolution of the jet.

We also made use of the 43 GHz VLBA map of the jet from Lister & Smith (2000) obtained at 1999 January 13, that is close to the MOJAVE epoch of 1999 January 2. This high frequency archival data provided better resolved jet structure compared to the 15 GHz data.

3.2 Error estimation and component identification

To decrease the degrees of freedom during the model-fit and to remain consistent through the epochs we used only circular Gaussian components to fit the brightness profile of the jet. In the analysis of the VLBA data by the MOJAVE group the core was fitted at several epochs by one elliptical component with axial ratio < 0.5. We fitted the core region by two circular components in each epoch without increasing the reduced χ^2 with respect to the MOJAVE analysis given in Lister et al. (2009). We also checked the higher frequency data of Lister & Smith (2000) from 1999 January 13 to clarify the presence of the northernmost component and concluded that it is visible at 43 GHz as well. The northernmost component is marked with 'CS' and the other jet-component in the core region is labelled by 'Cg' in accordance with the high frequency analysis of Lister & Smith (2000).

The fitted parameters were the position (x[mas], y[mas]), the integrated flux density (S_t [Jy]) and the full width at half maximum (FWHM) (d[mas]) of the Gaussian components. A representative image of the jet can be seen in Fig. 1. There is a prominent bend at an approximate core separation of 3 mas. Hough (2013) suggests that a similar bend seen in 3C 207 is related to the re-collimation zone in the jet of that source.

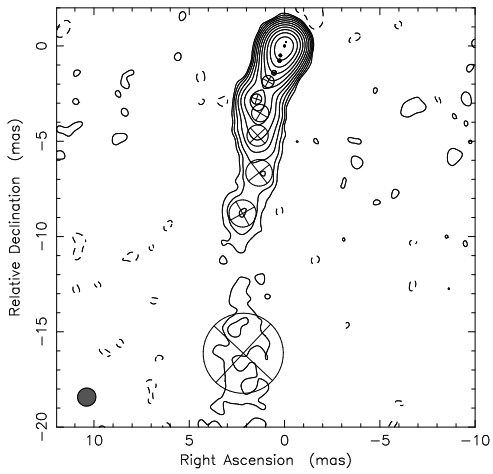

Figure 1. Model-fits to the 2013.06 epoch of MOJAVE observation of S5 1928+738 at 15 GHz. The core lies at $0, 0$ coordinates. Contours are in percent of the peak flux 2.18 Jy beam^{-1} and they increase by factors of two. The lowest contour level is 1.1 mJy beam^{-1} (0.05 percent of the peak flux). The off-source rms noise is 0.16 mJy beam^{-1}. The restoring beam-size is shown in the bottom left corner of the image (0.9mas × 0.9mas). Each circle on the map corresponds to a model-fit component. Their sizes represent the FWHM of the fitted Gaussian. Tapered image was created in DIFMAP.

For each component the post-fit root mean square error (σ_p) was determined on the residual image after the jet components were extracted from the original map around the position of each component. The peak flux of the components (S_p) was estimated from S_t and d. With $\theta_{\rm min}$ and $\theta_{\rm maj}$ denoting the minor and major axis of the restoring beam, the beam size is given as $\theta = \sqrt{\theta^2_{\rm min} + \theta^2_{\rm maj}}$. Then the error of the integrated flux density can be given as (Schinzel 2011)

$$\sigma_t = \left(\sigma_p \cdot \sqrt{1 + SNR}\right) \sqrt{\left(1 + \frac{S_t^2}{S_p^2}\right)}, \qquad (1)$$

where $SNR = S_p/\sigma_p$. The error of the component width is

$$\sigma_d = \begin{cases} \sigma_p \cdot \sqrt{\theta^2 + d^2}/S_p, & \theta > d \\ \sigma_p \cdot d/S_p, & \theta \leqslant d. \end{cases} \qquad (2)$$

Concerning the estimation of the position error we followed the suggestion of Lister et al. (2009) and assumed that the uncertainties on the position of the fitted components are $\sim 10\%$ of the component size convolved with the beam size. Then the position errors are given as:

$$\sigma_x = 0.1 \cdot \sqrt{\theta_x^2 + d^2}, \qquad (3)$$

$$\sigma_y = 0.1 \cdot \sqrt{\theta_y^2 + d^2}, \qquad (4)$$

where θ_x and θ_y are beam projected to the x and y axis, respectively. For our full sample containing even the faintest components, we estimate the average errors of the integrated

[1] http://www.physics.purdue.edu/astro/MOJAVE/

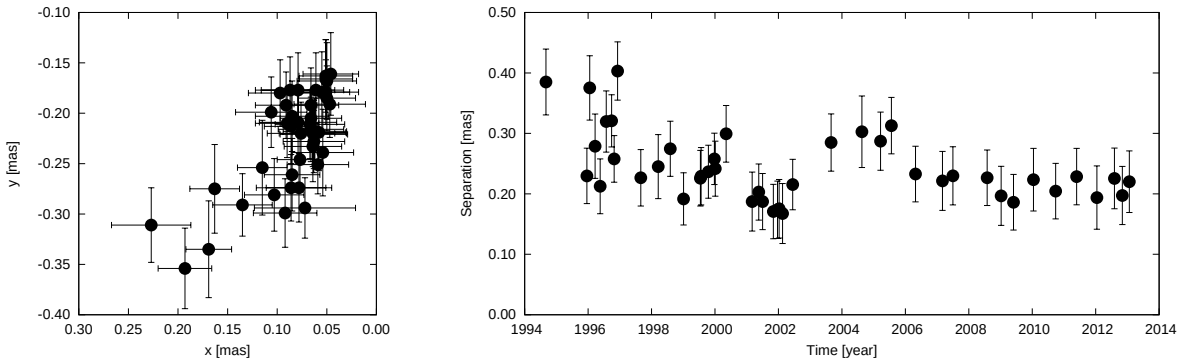

Figure 2. *Left*: Relative position of model-fit jet component Cg with respect to the position of model-fit jet component CS across the epochs at 15 GHz measured in the system, where East defines the x-axis and the North the y-axis. Cg appears to be stationary within the errors, except for 5 epochs implying the five most Eastern positions (1994.67, 1996.05, 1996.57, 1996.74, 1996.93). *Right*: Relative separation of Cg with respect to CS plotted against time.

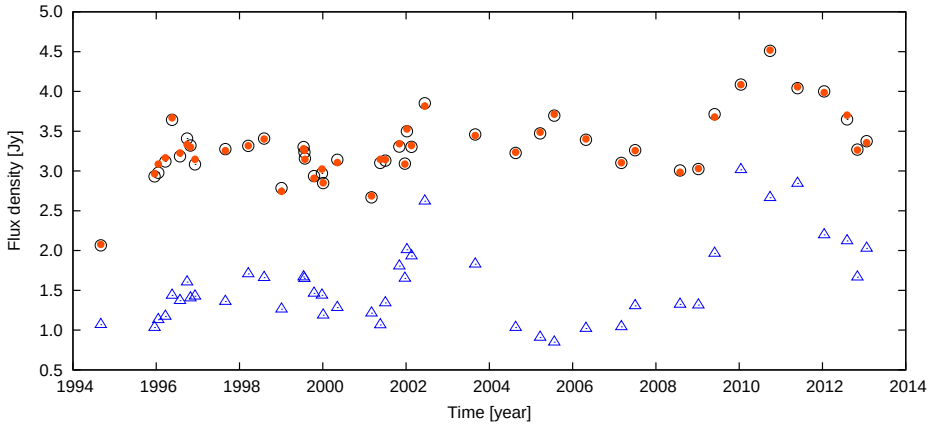

Figure 3. Flux density of the core region (combined flux densities of CS and Cg, blue triangle), total flux density of the jet measured by the MOJAVE (black open circle), total flux density of the components in the recent work (orange filled circle) plotted against time.

Table 1. Summary of the 15 GHz image parameters. (1) epoch of the VLBA observation, (2) VLBA experiment code, (3)–(4) FWHM minor and major axis of the restoring beam, respectively, (5) position angle of the major axis of the restoring beam measured from North through East, (6) rms noise of the image, (7) reduced χ^2 of the DIFMAP model-fit, (8) number of the components in the model. The full table is available in electronic format online.

Epoch (1)	VLBA Code (2)	B_{min} [mas] (3)	B_{maj} [mas] (4)	B_{PA} [°] (5)	rms mJy bm^{-1} (6)	Red. χ^2 (7)	Comp. Number (8)
1994 Aug 31	BZ004	0.67	0.76	-67	0.4	1.21	7
1995 Dec 15	BK37A	0.53	0.76	12	0.7	0.39	11
1996 Jan 19	BR034	0.44	1.00	-9	0.6	1.16	11
1996 Mar 22	BR034B	0.46	1.08	-16	0.4	1.01	11
1996 May 16	BK037B	0.52	0.83	-39	0.3	1.39	11
1996 Jul 27	BR034D	0.48	0.97	-16	0.4	2.55	10
1996 Sep 27	BR034E	0.47	0.91	-43	0.4	1.19	8
1996 Oct 27	BK037D	0.42	0.65	22	0.5	0.85	11

flux densities, positions and widths to be 20%, 8% and 12%, respectively.

The positions of the components can be most reliably determined for the most compact features. However, the larger the core separations, the larger the FWHM of the fitted components; therefore, the positional uncertainties increase as a function of the core distance. The identification of the outer jet shape is thus difficult.

Finally we cross-identified components across different epochs by requiring a smooth temporal change for the separation with respect to the core, the flux density, and the FWHM of the fitted Gaussian. The components are labelled with letter 'C' and a number, so that the larger number

Table 2. Circular Gaussian model-fit results for S5 1928+738. (1) epoch of observation, (2) flux density, (3)–(4) position of the component center with respect to the core, (5) FWHM, (6) jet-component identification. The full table is available in electronic format online.

Epoch [yr]	Flux density [Jy]	x [mas]	y [mas]	d [mas]	CO
1994.67	0.606 ± 0.044	0.000 ± 0.040	0.000 ± 0.037	0.145 ± 0.003	CS
	0.462 ± 0.045	0.227 ± 0.040	-0.311 ± 0.037	0.144 ± 0.005	Cg
	0.407 ± 0.042	0.561 ± 0.048	-1.238 ± 0.045	0.301 ± 0.007	C7
	0.408 ± 0.042	0.258 ± 0.051	-1.613 ± 0.049	0.350 ± 0.007	C6
	0.078 ± 0.020	1.153 ± 0.087	-3.282 ± 0.086	0.789 ± 0.064	C3
	0.038 ± 0.022	2.203 ± 0.206	-7.417 ± 0.206	2.029 ± 0.580	C2
	0.035 ± 0.012	2.675 ± 0.142	-10.212 ± 0.141	1.366 ± 0.175	C1

denotes the closest component to the core. The six jet components labelled with B1-B6 each appear in one epoch only. They cannot be followed through several epochs in a similar way to the standalone components marked as C.

The MOJAVE survey does not consist of phase-referenced observations, therefore there is no absolute positional information. To study the movement of the components, one has to choose a reference point. This reference point is usually the so-called core, which is assumed to be stationary. In the case of our model-fit of S5 1928+738, we have chosen the northernmost component (denoted by CS) as the core. This choice will be revisited and confirmed in Section 3.3. The parameters of the model-fit components are given in Table 2.

3.3 The behaviour of the jet

In addition to the core, 10-12 components can be identified at 15 GHz during the almost 20 years of radio observations. Most of the components are moving away from the core CS except Cg, which appears at nearly constant position with respect to the core (see Fig. 2). In the first few epochs, though, there is an apparent shift in its position. This can originate from projection effects, or observational effects. The latter possibility is related to the fact, that in these first few epochs the beam of the array was significantly different, more elliptical than in later epochs.

We calculated the linear proper motion of the components. The maximal proper motion obtained in the jet is $\mu_{\rm max} = 0.43 \pm 0.02$ mas yr^{-1} that is in excellent agreement with the maximal proper motion 0.43 ± 0.01 mas yr^{-1} by Lister et al. (2013). We note, however, the fastest component in our analysis is C3 (at an average core distance 6 mas), while the fastest component in the analysis of Lister et al. (2013) is the outermost component. Most probably the different choice of the reference point and the slightly different component identifications led to this difference between the two analysis.

The standard theory of the superluminal motion yields a connection between the apparent speed ($\beta_{\rm app}$), the intrinsic jet speed ($\beta_{\rm jet}$), and the inclination angle (ι):

$$\beta_{\rm app} = \frac{\beta_{\rm jet} \sin\iota}{(1 - \beta_{\rm jet}\cos\iota)}. \quad (5)$$

Taking the largest observed proper motion of $\mu_{\rm max} = 0.43 \pm 0.02$ mas yr^{-1}, the maximum apparent velocity seen in the jet is $\beta_{\rm app} \approx 8.1$c and therefore the lower limit of the Lorentz factor is $\Gamma_{\rm min} \approx 8.1$. The minimal intrinsic jet velocity is $\beta_{\rm jet} = 0.992$c, and the corresponding critical inclination angle, at which the apparent velocity is maximum, is $\iota_{\rm c,max} \approx 7^\circ$.

The other consequence of the Doppler boosting is that the apparent brightness temperature $T_{\rm b}$ can exceed the limiting intrinsic brightness temperature $T_{\rm int}$. In case of VLBI components the brightness temperature is calculated as (e.g. Condon et al. 1982):

$$T_{\rm b,VLBI}[{\rm K}] = 1.22 \cdot 10^{12}(1+z)\frac{S_\nu}{\theta^2\nu^2}, \quad (6)$$

where S_ν[Jy] is the flux density, θ[mas] is the FWHM of the component, and ν[GHz] is the observing frequency. We calculated $T_{\rm b,VLBI}$ for the brightest component in those epochs, at which the FWHM of this component was larger than 0.05 mas (roughly one tenth of the beam size). The apparent and intrinsic brightness temperatures are related to each other as $T_{\rm b} = \delta T_{\rm int}$, where $\delta = \Gamma^{-1}(1-\beta_{\rm jet}\cos\iota)^{-1}$ is the Doppler factor. We use $T_{\rm int} \approx 10^{11}$K as the maximal limit on the particle temperature (Lähteenmäki et al. 1999), at which the Compton catastrophe occurs. Thus the average Doppler factor becomes $\delta_{\rm VLBI} \approx 8.5$. Using the values derived from the jet kinematics, $\Gamma = 8.1$, $\beta = 0.992$, and $\iota = 7^\circ$, the Doppler factor is estimated to be $\delta \approx 8$, that is in good agreement with the Doppler factor derived from the brightness temperature of the components.

Considering this result and the large number of the observed jet-components having proper motion estimates in S5 1928+738, we expect that the bulk motion in the jet is not significantly faster than it is indicated by the observed maximum apparent velocity 8.1c. We adopt the above value of the inclination angle as initial value in the jet-fitting presented in Section 4.2.

The component Cg is the brightest in 32 out of 45 epochs. The behaviour of the Cg component raises the question whether the northernmost component CS is indeed the core or if it should be Cg instead. In the following, we discuss the components Cg and CS. If we assume that Cg is the core, then CS could be regarded as part of the counter-jet. In that case, assuming that the jet and counter-jet are symmetrical and have an intrinsic jet velocity of $\beta = 0.992$, an inclination angle of $\iota = 7.0^\circ$, a flat spectral index of $\alpha_{\rm 182MHz-8.4GHz} = -0.05$ (Healey et al. 2007), and a continuous jet with the parameter n=2 (Scheuer & Readhead 1979), we can calculate the jet counter-jet ratio as

$$R = \left(\frac{1+\beta\cos\iota}{1-\beta\cos\iota}\right)^{(n+\alpha)} \approx 13000. \quad (7)$$

This implies that for CS to be part of the counter-jet and be

observable it needs to be intrinsically 13000 times brighter than the jet. As this is not physically plausible, we conclude that the CS is not part of the counter-jet, but rather is the core.

The flux densities of the core region, the total flux density of the jet measured by the MOJAVE and from our model-fit process are displayed in Fig. 3. It can be seen that the flux variation of the core region dominates the total flux density across the epochs. The flux density variations in the core region are suggestive of periodic behaviour, indicating a variable jet-source at the jet base. The jet components are expanding with increasing core separation, as expected from their adiabatic cooling that occurs as they move away from the core.

We note, that the sampling of the total flux density is nearly homogeneous except for the first epoch, when there is a time gap of 1.3 year between the first and the second epochs. Because the flux curve is poorly determined between 1994-1996 and we can identify only 7 components in the first epoch, we excluded the first epoch (1994.67) from our jet analysis presented in Section 4.2.

4 GEOMETRICAL MODEL FOR THE JET

In this section we will use a geometric model to describe the jet morphology as developed by Nakamura et al. (2001). They modelled the AGN radio jets by 3D magnetohydrodynamic (MHD) simulations based on the Sweeping Magnetic-Twist model. According to this a Poynting flux of torsional Alfvén wave train produced in the interaction of the rotating accretion disk and the large scale magnetic field results in a slender jet shape by the sweeping pinch effect. Wiggled structures in the jets are produced by the helical kink instability, as the torsional Alfvén wave train encounters a domain of reduced Alfvén velocity, where the toroidal component of the field accumulates, resulting in a helical structure of the jet.

In what follows, we describe the mathematical formalism used to fit the jet geometry (Section 4.1), and the application of this model to the jet (Section 4.2).

4.1 Revealing the shape of the jet

Following Nakamura et al. (2001), we model the jet of S5 1928+738 with a helical structure and describe the jet pattern with a conical helix in the following way:

$$\begin{aligned} x_{\rm jet} &= \frac{b}{2\pi} u \cos u, \\ y_{\rm jet} &= \frac{b}{2\pi} u \sin u, \\ z_{\rm jet} &= \frac{a}{2\pi} u, \end{aligned} \tag{8}$$

where u is the polar angle measured in the plane perpendicular to the jet cone axis, and a and b are the axial and radial growth rates of the jet per turn, respectively. We use the following coordinate system where the x and y axes are in the plane of the sky and

x axis points to East,
y axis points to North,
z axis is the direction of the LOS.

The projection of the jet onto the xy plane can be carried out by two rotational matrices. The $R_{+\iota_0}$ matrix

$$R_{+\iota_0} = \begin{pmatrix} \cos\iota_0 & 0 & \sin\iota_0 \\ 0 & 1 & 0 \\ -\sin\iota_0 & 0 & \cos\iota_0 \end{pmatrix} \tag{9}$$

rotates the structure around the y axis from the LOS toward the plane of the sky with ι_0 angle, that is the inclination angle between the LOS and the jet axis. The 0 index refers to the angles of the jet geometrical axis. If the jet geometrical axis lies in the plane of the sky, ι_0 equals 90°, if the jet axis points exactly to the observer, ι_0 equals 0°. The $R_{+\lambda_0}$ matrix

$$R_{+\lambda_0} = \begin{pmatrix} \cos\lambda_0 & -\sin\lambda_0 & 0 \\ \sin\lambda_0 & \cos\lambda_0 & 0 \\ 0 & 0 & 1 \end{pmatrix} \tag{10}$$

rotates the structure around the z axis with λ_0, that is the position angle of the jet symmetry axis measured in the plane of the sky with respect to the y axis. Applying the rotational matrices on the helix shape, the projected helical structure in 2D becomes:

$$x^p_{\rm jet}(u) = F(u)\cos(\lambda_0) - G(u)\sin(\lambda_0) \tag{11}$$

$$y^p_{\rm jet}(u) = F(u)\sin(\lambda_0) + G(u)\cos(\lambda_0) \tag{12}$$

where

$$F(u) = \frac{b}{2\pi} u \cos(u-\phi)\cos(\iota_0) + \frac{a}{2\pi} u \sin(\iota_0) \tag{13}$$

$$G(u) = \frac{b}{2\pi} u \sin(u-\phi) \tag{14}$$

and ϕ is an initial phase.
The intrinsic half-opening angle of the cone ($\psi^{\rm int}$) can be given by the radial and axial increments as

$$\tan(\psi^{\rm int}) = b/a. \tag{15}$$

The apparent half-opening angle of the cone ($\psi^{\rm obs}$) is related to $\psi^{\rm int}$ as

$$\psi^{\rm obs}(0^\circ < \iota_0 < 90^\circ) = \frac{\psi^{\rm int}}{\sin\iota_0}. \tag{16}$$

4.2 Applying the model to the jet of S5 1928+738

We deal with the above described helical jet shape and present the application of the geometrical model. In the present context, we do not mark the components, but just assume that they are part of the jet and reveal the jet shape in one epoch; we fit the jet as a whole instead of fitting the individual components' path.

The compact jet of S5 1928+738 extends over 15 mas. Because roughly half of the jet-components lie within core separation of 2 mas in every epoch and dominate the flux density, and because the inner jet (core separation $\leqq$ 2 mas) can be more precisely model-fitted (see Section 3.2) than the outer jet (core separation $>$ 2 mas), in the following we deal only with the inner part of jet. In addition to the above reasoning, any precession of the jet due to a binary would primarily affect the inner jet, with the effects of the precession being dampened as the core separation increases.

For resolved jets, there is evidence for non-zero opening angles. Perucho et al. (2012) analysed multi-epoch VLBI data of the radio jet in the quasar S5 0836+710 at different

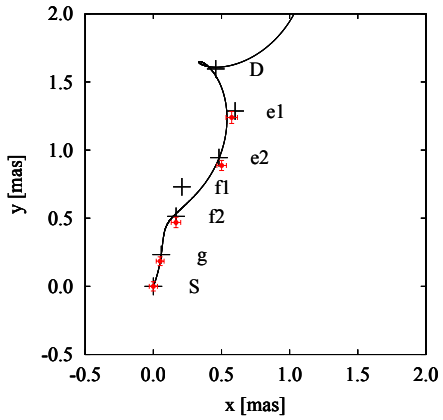

Figure 4. Black crosses denote the 43 GHz model components derived by Lister & Smith (2000) (their sizes are not representative of the errors), red dots with error bars denote the 15 GHz model components. In the figure, North is oriented towards negative y values. We complement the data by five of the seven component positions identified at 15 GHz. The black curve represents the "starting jet model" (see Section 4.2) fitted to the 43 GHz data.

Table 3. Starting parameters for the geometrical model obtained by jet component positions at 43 GHz (Lister & Smith 2000). The inclination angle, ι_0, was calculated from the maximum observed apparent velocity (see Section 3.3).

$\iota_0[^\circ]$	$\lambda_0[^\circ]$	a [mas]	b [mas]
7.00	160 ± 2	10.6 ± 0.4	0.18 ± 0.06

frequencies and found that the jet opening angles are similar at all the used frequencies: 1.6, 2, 5, 8, 15, 22, and 43 GHz.

In accordance with the finding that the opening angle does not depend on the typical VLBI observing frequencies (e.g. Perucho et al. 2012, and references therein), we use the 43 GHz data to derive the intrinsic half-opening angle of the jet as an input parameter for modelling of the 15 GHz datasets. The model-fit results for the inner 2 mas of the jet at 43 GHz data given by Lister & Smith (2000) are in good agreement with our model-fit results of the most closely separated 15 GHz data (see Fig. 4) but contain more components, describing the jet shape more precisely. Thus we set up a starting model of the helical jet by fitting Eq. (11) and Eq. (12) on the component-positions of the inner jet measured at 43 GHz.

The degeneracy between the inclination angle and the intrinsic half-opening angle does not allow for these parameters to be fitted together, see Eq. (16). Therefore, one needs to estimate one of these angles independently. In Section 3.3 we derived the inclination angle $\iota = 7.0^\circ$ from the apparent velocity seen in the jet. The method is independent from the geometrical model and therefore we fix the inclination of the jet axis $\iota_0 = 7.0^\circ$ in the starting model at 43 GHz.

We fitted the 43 GHz components' positions with the conical helix described by Eq. (11) and Eq. (12). The resulting parameters of the fit are given in Table 3. Based on our parametric fit, the jet parameter $\Gamma\psi^{\rm int}$ is 0.14 ± 0.05, using $\Gamma = 8.1$ and $\psi^{\rm int} = \arctan(b/a) = 0.017$ rad $\pm\, 0.006$ rad. This value is in good agreement with the general value given by Pushkarev et al. (2009).

Table 4. The inclination and position angles of the jet axis obtained from the parametric fit on the 15 GHz data. The full table is available in electronic format online.

Epoch	λ_0	ι_0
1995.96	153.05 ± 6.38	8.20 ± 1.13
1996.05	153.67 ± 4.75	10.14 ± 1.23
1996.22	154.41 ± 5.36	9.26 ± 1.25
1996.38	153.04 ± 6.33	9.04 ± 1.07
1996.57	158.42 ± 7.40	9.70 ± 1.77
1996.74	152.34 ± 6.06	10.08 ± 1.14
1996.82	158.09 ± 4.30	7.17 ± 0.68
1996.93	155.77 ± 5.72	7.57 ± 1.00

Next we fitted the measured component positions in all epochs of the MOJAVE data with Eq. (11) and Eq. (12). We used a and b parameters obtained from the 43 GHz fit as fixed parameters. We allow the inclination and position angle to vary from the starting values given in Table 3. The resulting time series of the inclination and position angle of the jet axis are given in Table 4 and plotted in the lower two panels of Fig. 5. The individual components can have smaller or larger inclination than the jet axis has, as the plasma flows around the jet axis, along the magnetic helix.

As it can be seen from Fig. 5, the flux density, the inclination, and the position angle vary in a periodic way around slowly changing average values. The orbital motion of the jet emitter BH explains the periodic behaviour. Our BBH model takes into account the monotonic change as well, via the spin-orbit precession. Therefore we fitted a harmonic function extended with a monotonic changing term to the data, that reflects a periodic variation with time while also allowing for linear drift in the average values:

$$F(t) = A_0(F) + A_1(F)\sin\left(\frac{2\pi}{T(F)}t - \phi(F)\right) + A_2(F)t, \quad (17)$$

$$\iota_0(t) = A_0(\iota_0) + A_1(\iota_0)\sin\left(\frac{2\pi}{T(\iota_0)}t - \phi(\iota_0)\right) + A_2(\iota_0)t, \quad (18)$$

$$\lambda_0(t) = A_0(\lambda_0) + A_1(\lambda_0)\sin\left(\frac{2\pi}{T(\lambda_0)}t - \phi(\lambda_0)\right) + A_2(\lambda_0)t. \quad (19)$$

The numerical value of the parameters in the above functions were obtained by performing a non-linear least squares fitting on the time-variation of the corresponding jet-quantities using the Levenberg-Marquardt algorithm, such that the χ^2 was minimized during the fitting. The coefficients of Eq. (17), Eq. (18), Eq. (19), and the corresponding χ^2 values are given in Table 5.

In Section 5 we will use the inclination parametrization given by Eq. (18) to deduce the binary parameters. For this reason a hypothesis test was carried out to check whether the function given in Eq. (18), predicted by our BBH model, is consistent with the inclination variation of the jet axis. The null-hypothesis states that the inclination-variations of the jet axis at different epochs are drawn from a random distribution. The alternative hypothesis states that the variations are drawn from a distribution described by Eq. (18). We checked the probability $P(\chi^2 <= {\chi^2}_{\rm cv})$, where ${\chi^2}_{cv}$ is 20.94 for ι_0, by performing a non-parametric Monte-Carlo test. We produced 10000 new time-series by randomly mixing the original 44 inclination data points and then fitted these with Eq. (18). The test gave $\chi^2 < \chi^2_{\rm cv}$ in 24 cases

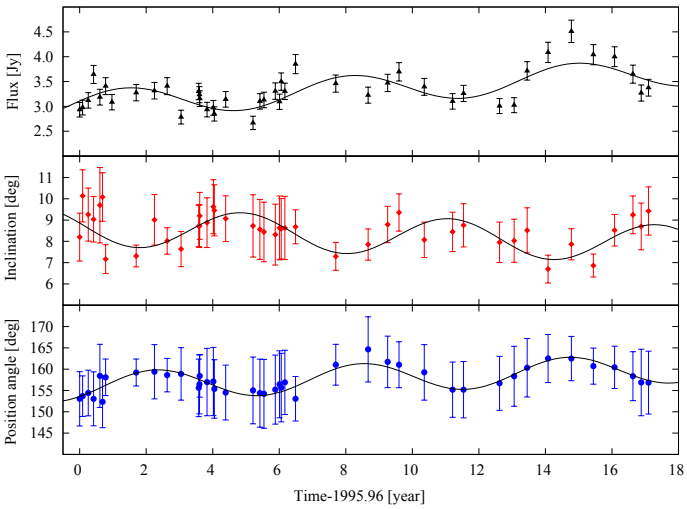

Figure 5. Total flux density of the jet at 15 GHz (top), inclination (middle) and position angle (bottom) of the jet geometrical axis plotted against time. The flux variability refers to the jet as a whole. The error bars represent the error of the angles after the parametric fit given by Eq. (11) and Eq. (12) on the xy positions of the inner jet. The curves are analytical fits to characterize the periodicities and linear trends in the time-series (parameters of the curves are given in Table 5).

Table 5. The parameters of the analytical fits to the time-series of the total flux densities at 15 GHz, inclination angles, and position angles (their mathematical form given in Eq. (18) and Eq. (19)) are displayed. The total χ^2 values are also indicated (the degrees of freedom are $N = 39$ for all cases).

F, $\chi^2 = 22.20$				
A_0[Jy]	A_1[Jy]	A_2 [Jy yr^{-1}]	T [yr]	ϕ [°]
3.03 ± 0.06	0.29 ± 0.06	0.04 ± 0.01	6.74 ± 0.24	-15.44 ± 16.33
ι_0, $\chi^2 = 20.94$				
A_0[°]	A_1[°]	A_2 [°yr^{-1}]	T [yr]	ϕ [°]
8.67 ± 0.19	0.89 ± 0.17	-0.05 ± 0.02	6.22 ± 0.19	11.95 ± 15.01
λ_0, $\chi^2 = 5.82$				
A_0[°]	A_1[°]	A_2 [°yr^{-1}]	T [yr]	ϕ [°]
155.90 ± 0.36	3.39 ± 0.33	0.24 ± 0.04	6.20± 0.10	42.99± 7.83

implying $P(\chi^2 < \chi^2_{\rm cv}) \approx 0.0024$. Thus we rejected the null-hypothesis, and accepted that the fit mirrors real variations. We can conclude that our BBH model (periodic variation due to orbital motion, and monotonic change due to spin-orbit precession) is able to explain the inclination angle variation of the jet axis.

The variation in the inclination angle of the jet axis permits that ι_0 changes between approximately 7° and 9°, additionally the non-zero jet opening angle of $\psi^{\rm int}$ allows the inclination angle of the components to be between 6° and 10°. The minimal and maximal apparent velocities are 3.4c and 6.6c in the first 2 mas part of the jet, respectively. Assuming a constant Lorentz-factor of $\Gamma = 8.1$ for the whole jet, the observed apparent velocities cannot be reproduced. Changes in the intrinsic jet velocity are often observed in extragalactic jets (e.g. Asada et al. 2014, and references therein). In the present case, the intrinsic jet velocity should be between $\approx 0.965c$ and $\approx 0.990c$ allowing a variable $\beta_{\rm jet}$.

4.3 Radio flux density variability

The total flux density of the jet is plotted against time on the upper panel in Fig. 5. We fitted the data by a function similar to those given for the inclination and position angles. The resulting coefficients are given in the first line of Table 5. The total flux density variability can be described in a way that it is brighter (fainter) when the average inclination angle of the jet axis is smaller (larger). This points towards variable Doppler boosting as the reason behind the observed radio flux variability.

In the case of S5 1928+738, the total flux density variation at 15 GHz is dominated by components Cg and CS. The flux variability of the core region indicates a six year periodicity, similar to the period of the inclination variation of the jet axis. The monotonic decreasing value of the average inclination angle suggests that the jet axis moves closer and closer to the line of sight. This slow reorientation of the inner jet is consistent with the observed long-term brightening of the jet.

On the other hand, the sharp peaks in the flux density of the core region (at epochs 2002.45 yr and 2010.04 yr) could also be attributed to component ejections, following the shock-in-jet model of Marscher & Gear (1985) and Björnsson & Aslaksen (2000). The shock-shock interaction, when a newly ejected component travels through the core region of the jet may cause the observed brightening. The components having closest ejection epochs to the peaks are C12 ($t_{\rm ej,C12} = (2000.74 \pm 0.19)$yr) and C16

($t_{\rm ej,C16} = (2008.83 \pm 0.20)$yr). If we assume that the components maintained their observed speed ($\mu_{C12} = 0.180 \pm 0.009$ mas yr^{-1} and $\mu_{\rm C16} = 0.180 \pm 0.013$ mas yr^{-1}) after their ejections, they arrived at the position of Cg approximately at the time of the flux density increase. In this scenario Cg is actually a standing shock zone in the jet, that brightens as a powerful moving shock (components C12 and C16) moves through it.

It is plausible that the radio flux variability of the core region of S5 1928+738 at 15 GHz has a composite origin. The component ejections can explain the periodic component of the flux variability. On the other hand, its linear component can be attributed to the manifestation of the spin precession of the jet emitter black hole through the Doppler boosting of the emitted light.

5 SMBH BINARY IN THE CENTRAL PART OF THE S5 1928+738

In this section we connect the presented jet behaviour to a dynamical model of merging SMBH binary. Following Roos et al. (1993) we assume that the periodic change of the polar angle of the jet axis is generated by a hidden SMBH binary at the base of the jet. Then we identify the linear trend in the evolution of the average angles by the slow reorientation of the spin of the jet emitter BH due to the spin-orbit precession. Based on the above assumptions we calculate the binary parameters. Note, that in this section we do not consider the helix described in the geometrical model, rather we consider its axis that itself spirals due to the orbital motion. This secondary spiral structure is revealed by the periodically changing inclination and position angles of the jet axis (see Fig. 5).

5.1 Earlier estimation of total mass, binary separation and orbital period

Once the immediate environment of the central mass becomes sufficiently active to radiate like a QSO, its luminosity L approaches the Eddington luminosity $L_{\rm E}$ (for a review see e.g. Schneider 2006). Roos et al. (1993) adopted a total mass of $m_{\rm I} \approx 10^8 M_\odot$ for the SMBH binary hosted in S5 1928+738, based on the Eddington limit and assuming a bolometric luminosity of $8.15 \cdot 10^{45}$ergs^{-1}. Further mass estimates have been published by other authors, constraining the total mass of the SMBH binary at around $10^8 M_\odot$ (Kelly & Bechtold 2007; Liu et al. 2006). An order of magnitude higher SMBH mass was estimated by Cao & Jiang (2002). With the large uncertainties and intrinsic scatter of SMBH mass estimates from different methods noted, here we adopt $m \approx 8.13 \times 10^8 M_\odot$ derived by Woo & Urry (2002) from the black hole mass-AGN continuum luminosity scaling relation, which in turn is based on the reverberation mapping technique.

Hummel et al. (1992) fitted a moving sine-wave on the component positions of the mas-scale jet of S5 1928+738 obtaining a wavelength of ~ 1.06 mas, phase shift of ~ 0.28 mas yr^{-1} and amplitude of ~ 0.09 mas. Roos et al. (1993) estimated the orbital period of the binary as the wavelength of this sine-wave divided by its phase-shift, yielding an orbital period of ~ 2.9 yr, measured in the rest frame of the source. By considering the total mass $m \sim 10^8 M_\odot$ and the orbital period ~ 2.9 yr, Roos et al. (1993) calculated the binary separation of $r \approx 0.003$ pc based on Kepler's third law. Compared to these, we adopt a refined model, paying attention to details related to the spin.

5.2 Binary parameters

We consider two SMBHs orbiting each other with total mass $m = m_1 + m_2$ and mass ratio $\nu = m_2/m_1 < 1$. The equation of motion is (Kidder 1995):

$$\frac{d^2\mathbf{r}}{dt^2} = -\frac{m\mathbf{r}}{r^3}\left(1 + \mathcal{O}(\varepsilon) + \mathcal{O}(\varepsilon^{1.5}) + \mathcal{O}(\varepsilon^2) + \mathcal{O}(\varepsilon^{2.5}) + ...\right), \tag{20}$$

where $\mathbf{r}$ is the binary separation, $r = |\mathbf{r}|$, $\varepsilon = Gmc^{-2}r^{-1}$ is the post-Newtonian (PN) parameter and $\mathcal{O}(\varepsilon^n)$ represents the nth PN order. The radial evolution of the binary is characterized to Newtonian order by the total mass m, the orbital period T and the separation r, only two of them being independent. To 1PN accuracy the mass ratio enters as a fourth parameter.

If the jet periodicities observed in S5 1928+738 are consequences of the orbital motion of the binary, then the separation can be calculated to Newtonian order as:

$$r = 0.29 \times (Gm)^{1/3} T^{2/3}, \tag{21}$$

where T is provided from the periodic component in the variation of the inclination $T(\iota_0)$, so that $T = T(\iota_0)(1+z)^{-1} = 4.78 \pm 0.14$ yr in the rest frame of the source. By employing the total mass estimate of Woo & Urry (2002) $m = 8.13 \times 10^8 M_\odot$, Eq. (21) implies the separation $r = 0.0128 \pm 0.0003$ pc and consequently the PN parameter $\varepsilon \approx 0.003$.

After the gravitational radiation becomes the dominant dissipative effect over the dynamical friction, the evolution of the compact binary passes through three phases, the inspiral, the plunge, and the ring-down. The $\varepsilon \approx 0.003$ value of the PN parameter found in S5 1928+738 indicates that the SMBH binary is in the inspiral phase, typically encompassing the range $0.001 < \varepsilon < 0.1$ (Gergely & Biermann 2009; Levin et al. 2011).

Up to 2PN order the merger dynamics are conservative, the constants of motion being the total energy E and the angular momentum vector $\mathbf{J} = \mathbf{S_1} + \mathbf{S_2} + \mathbf{L}$, where $\mathbf{L}$ is the orbital angular momentum, $\mathbf{S_1}$ is the spin of the dominant SMBH and $\mathbf{S_2}$ is the spin of the secondary SMBH. The SMBH spins obey precessional motion (Barker & O'Connell 1975, 1979):

$$\dot{\mathbf{S}}_\mathbf{i} = \Omega_i \times \mathbf{S_i}, \tag{22}$$

where index i refers to the first and second member of the binary, the angular velocity Ω_i of the ith spin $\mathbf{S_i}$ contains up to 2PN order spin-orbit (1.5PN), spin-spin (2PN), and quadrupole momentum contributions (2PN). For the typical mass ratio only the dominant spin is important (Gergely & Biermann 2009), and the spin of the secondary black hole $\mathbf{S_2}$ can be neglected. The 2PN effects are also neglected. In the one-spin case the dominant spin $\mathbf{S}$ precesses around $\mathbf{J}$ with the angular velocity (Gergely & Biermann

2009):

$$\Omega_{\rm p} = \frac{2c^3}{Gm}\varepsilon^{5/2}\frac{\nu}{(1+\nu)^2}. \quad (23)$$

Reorientation of the spin of the dominant SMBH should consequently cause variations in the jet direction. We identify the linear change in the direction of jet axis of S5 1928+738 with the spin precession of the dominant SMBH.

Once the binary evolution has progressed into the inspiral stage, the black holes approach further and coalescence is expected within the gravitational time-scale of the system (Gergely & Biermann 2009):

$$T_{\rm merger} = \frac{5Gm}{32c^3}\varepsilon^{-4}\frac{(1+\nu)^2}{\nu}, \quad (24)$$

due to gravitational wave emission. The semi-major axis and eccentricity of the elliptical orbits both decrease due to the emitted gravitational radiation, the latter occurring faster, hence circularizing the orbit (Peters 1964), what we assume hereafter.

Next we determine the mass ratio interval compatible with observations in our model. The orbital motion of the jet emitter black hole makes the jet geometrical axis wiggle about the spin with a half-opening angle ζ. This angle is the amplitude of the periodic component in $\iota_0(t)$ determined as $\zeta = A_1(\iota_0)(1+z)^{-1} = 0.68^\circ \pm 0.13^\circ$. It can be also expressed as:

$$\zeta = \arcsin\frac{v_1\cos\kappa}{v_{\rm jet}}, \quad (25)$$

where $v_1\cos\kappa$ is the component of the orbital velocity of the jet emitter BH perpendicular to the spin direction, κ represents the angle between the spin of the jet emitter black hole and the orbital angular momentum. Substituting the orbital velocity of the jet emitter black hole $\beta_1 = v_1 c^{-1} = \varepsilon^{1/2}\nu(1+\nu)^{-1}$, and the intrinsic jet velocity $\beta_{\rm jet}$ (both given in units of c) into the above equation, the angle κ can be expressed as:

$$\kappa = \arccos\frac{\beta_{\rm jet}\sin\zeta}{\varepsilon^{1/2}}\frac{1+\nu}{\nu}. \quad (26)$$

Substituting the known parameters into the above equation, the angle κ becomes a function of the mass ratio. We plot $\kappa(\nu)$ in Fig. 6. The parameter space is restricted below.

The SMBHs in the binary co-evolved in similar astrophysical environments, therefore it is plausible to assume that they have similar dimensionless spin parameter, hence $S_2/S_1 \approx \nu^2$. Values of $\nu > 1/3$ and consequently $S_2/S_1 > 0.1$ would allow for two pronounced jets in the system (morphologically like the X-shaped radio sources). Nevertheless there is no evidence of a double jet base in the jet, which would generate different families of component motions, indicating spins of comparable magnitude. Therefore we restrict the mass ratio to $\nu < 1/3$.

When the spin of a Kerr black hole is non-parallel to the orbital angular momentum, the spin-orbit interaction leads to orbital plane and spin precessions. The slow reorientation and brightening of the inner jet strongly supports such a precession, hence parallel dominant spin and orbital angular momentum configurations with $\kappa = 0^\circ$ are ruled out.

As it can be seen from Fig. 6., taking into account the 1σ error of the inclination amplitude $\mathrm{d}\zeta = 0.13^\circ$ and of the PN parameter $\mathrm{d}\varepsilon = 7\times10^{-5}$, the above arguments constrain the mass ratio to the range $\nu \in [0.21 : 1/3]$. We note, that the expected small change in $\beta_{\rm jet}$ along the jet ($\Delta \approx 0.03c$) would just slightly modify the limit on ν (see Eq. (25)). Then the spin-orbit precession period $T_{\rm SO} = 4852 \pm 646$ yr is estimated via Eq. (23) and the merger time $T_{\rm merger} = (1.44 \pm 0.19) \times 10^6$ yr is estimated via Eq. (24). The binary parameters are summarized in Table 6.

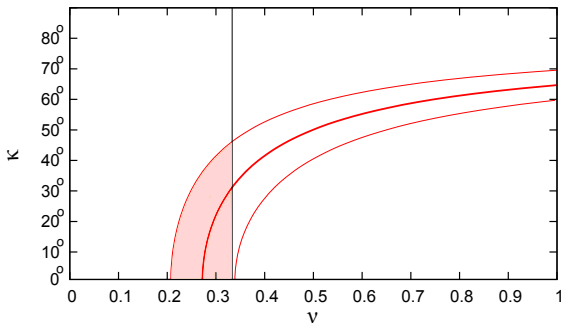

Figure 6. The thick solid line represents the function $\kappa(\nu)$ given by Eq. (26), with the upper and lower continuous lines representing the respective errors. The vertical solid line sets the upper limit of the typical mass ratio at $\nu = 1/3$ (a higher mass ratio would imply comparable spins, hence two jets, contradicting the observations). The shaded area indicates the parameter range allowed by observations of the jet. Although the available data on the function $\kappa(\nu)$ does not constrain the precession angle from below, a vanishing κ is not allowed, as it would switch off the spin-orbit precession.

Table 6. Binary parameters. ⋆:independent result by Woo & Urry (2002).

Total mass, m⋆ $[M_\odot]$	8.13×10^8
Orbital period, T [yr]	4.78 ± 0.14
Binary separation, r [pc]	0.0128 ± 0.0003
PN parameter, ε	≈ 0.003
Mass ratio, ν	$[0.21 : 1/3]$
Spin-orbit precession period, $T_{\rm SO}$ [yr]	4852 ± 646
Gravitational lifetime, $T_{\rm merger}$ [yr]	$(1.44 \pm 0.19) \times 10^6$

6 DISCUSSION AND CONCLUSIONS

In this paper we investigated the radio jet of S5 1928+738 based on calibrated data of the MOJAVE survey with focus on the perturbed jet ejection. Our analysis basically confirmed the model of Roos et al. (1993) which in turn was based on the jet analysis by Hummel et al. (1992) of a hidden SMBH binary at the jet base, causing the observed wiggling of the jet. The improvement upon this model, advanced in the present paper is the inclusion of the spin of the jet-producing black hole.

We developed a detailed geometrical model to describe the inner 2 mas of the jet by using the 43 GHz VLBA-map of Lister & Smith (2000). From that we obtained the inclination and position angle of the jet axis and the intrinsic half-opening angle of the conical helix. Then we fitted the geometric model to the 15 GHz VLBA data of almost twenty years. Three features of the jet have been revealed; (i) a conical helix shape, (ii) a periodical change in the direction

of its symmetry axis, (iii) a slow additional reorientation in the average direction of the jet. Our spinning binary black hole model naturally explained the simultaneous presence of properties (ii) and (iii), and (i) was attributed to the presence of helical kink instabilities.

Jet precession (iii) can be induced through the Bardeen-Petterson interaction between a viscous accretion disk and a spinning black hole (Bardeen & Petterson 1975), if the disk is misaligned compared to the equatorial plane of the black hole. However such a scenario cannot explain both (ii) and (iii). In an alternative scenario, the influence of the immediate environment could cause the wiggling of the jet. However, to explain the observed periodicities would require properly fine-tuned structures. So far there is no evidence for such periodic distribution of dense material close to the jet.

We adopted the total mass of the binary $m = 8.13 \times 10^8 M_\odot$ determined by Woo & Urry (2002) from the black hole mass-AGN continuum luminosity scaling relation (this value is different by a factor of 8.13 from the one adopted by Roos et al. 1993). The helical jet model with periodic jet axis and VLBI data implied the orbital period $T = 4.78 \pm 0.14$ yr (this is a factor of 1.59 larger than the value given by Roos et al. 1993). With these values we calculated the binary separation as $r = 0.0128 \pm 0.0003$ pc. These parameters imply that the SMBH binary is in the inspiral phase, but far from coalescence, with post-Newtonian parameter $\varepsilon \approx 0.003$.

Long-term monitoring of the radio jet allowed us to identify the linear trend in the evolution of the inclination and position angles of the jet axis, interpreted as arising from the spin-orbit precession of the jet emitter SMBH. The mass ratio most likely falls into the range $\nu \in [0.21 : 1/3]$. The spin-orbit precession period was identified as $T_{\rm SO} = 4852 \pm 646$ yr and the gravitational lifetime emerged as $T_{\rm merger} = (1.44 \pm 0.19) \times 10^6$ yr.

Although we cannot rule out that other models could explain the observed jet structure, we showed that the VLBI data of S5 1928+738, extending over almost twenty years is consistent with the model of a spinning binary black hole lying at the jet base, where the larger black hole has a spin detectable through its spin-orbit precession. Measurements of slow increase in the average flux density of the jet in the newest three epochs (2013.34, 2013.58 and 2013.96) further support the model, as such an increase is predicted by spin-orbit precession. Our study thus provides indications, for the first time from VLBI jet kinematics, for the spinning nature of the jet-emitting black hole.

As the MOJAVE survey is still ongoing, further data on S5 1928+738 may better constrain the parameters of the model. With a significantly increased amount of data in principle it would be possible to monitor higher order post-Newtonian effects too. Beyond spin induced precession, such an analysis could also reveal the magnitude of the spin, unavailable at the accuracy of the present analysis.

ACKNOWLEDGEMENTS

We thank the referee for helpful comments and suggestions. EK was partially supported by COST Action MP0905 "Black Holes in a Violent Universe". EK acknowledges financial support from the International Space Science Institute. During this research, KÉG and LÁG were supported by the European Union and the State of Hungary, co-financed by the European Social Fund in the framework of TÁMOP-4.2.4.A/2-11/1-2012-0001 "National Excellence Program". In the early stages of this research KÉG was supported by the Hungarian OTKA grant K 104539 and LÁG by EU grant TÁMOP-4.2.2.A-11/1/KONV-2012-0060 and the Japan Society for the Promotion of Science. MK was supported by the National Research Foundation of Korea (NRF) grant, No. 2008-0060544, funded by the Korea government (MSIP). This research has made use of data from the MOJAVE database that is maintained by the MOJAVE team. The Very Long Baseline Array (VLBA) is an instrument of the National Radio Astronomy Observatory (NRAO). The National Radio Astronomy Observatory is a facility of the National Science Foundation operated under cooperative agreement by Associated Universities, Inc.

REFERENCES

Abraham R. G., 1999, in Barnes J. E., Sanders D. B., eds, Galaxy Interactions at Low and High Redshift Vol. 186 of IAU Symposium, A Review of High-Redshift Merger Observations. p. 11
Alberdi A. et al., 1997, A&A, 327, 513
Asada K., Nakamura M., Doi A., Nagai H., Inoue M., 2014, ApJ, 781, 2
Bardeen J. M., Petterson J. A., 1975, ApJ, 195, 65
Barker B. M., O'Connell R. F., 1975, PhRvD, 12, 329
Barker B. M., O'Connell R. F., 1979, GReGr, 11, 149
Begelman M. C., Blandford R. D., Rees M. J., 1980, Nature, 287, 307
Begelman M. C., Blandford R. D., Rees M. J., 1984, RvMP, 56, 255
Binney J., Tremaine S., 1987, Galactic dynamics, Princeton Univ. Press, Princeton
Björnsson C. -I., Aslaksen T., 2000, GReGr, ApJ, 533, 787
Blandford R. D., 1986, in Swarup G., Kapahi V. K., eds, Quasars Vol. 119 of IAU Symposium, Black hole models of quasars. p. 359
Blandford R. D., Znajek R. L., 1977, MNRAS, 179, 433
Bon E. et al., 2012, ApJ, 759, 118
Britzen S. et al., 2009, A&A, 508, 1205
Britzen S. et al., 2010, A&A, 511, 57
Britzen S., Roland J., Laskar J., Kokkotas K., Campbell R. M., Witzel A., 2001, A&A, 374, 784
Britzen S. et al., 2008, A&A, 484, 119
Camenzind M., Krockenberger M., 1992, A&A, 255, 59
Cao, X., Jiang D. R., 2002, MNRAS, 331, 111
Caproni A., Abraham Z., 2004, MNRAS, 349, 1218
Caproni A., Abraham Z., Monteiro H., 2013, MNRAS, 428, 280
Condon J. J., Condon M. A., Gisler G., Puschell J. J., 1982, ApJ, 252, 102
Deane R. P. et al., 2014, Nature, 511, 57
Fan J. H. et al., 2007, A&A, 462, 547
Gergely L. Á., 2010a, PhRvD, 82, 104031
Gergely L. Á., 2010b, PhRvD, 81, 084025
Gergely L. Á., Biermann P. L., 2009, ApJ, 697, 1621
Hardee P. E., Stone J. M., 1997, ApJ, 483, 121

Healey S. E., Romani R. W., Taylor G. B., Sadler E. M., Ricci R., Murphy T., Ulvestad J. S., Winn J. N., 2007, ApJS, 171, 61
Hough D., 2013, European Physical Journal Web of Conferences, p. 8009
Hummel C. A., Muxlow T. W. B., Krichbaum T. P., Quirrenbach A., Schalinski C. J., Witzel A., Johnston K. J., 1992, A&A, 266, 93
Johnston K. J., Simon R. S., Eckart A., Biermann P., Schalinski C., Witzel A., Strom R. G., 1987, ApJ, 313, L85
Karouzos M., Britzen S., Witzel A., Zensus A. J., Eckart A., 2012a, AN, 333, 417
Karouzos M., Britzen S., Witzel A., Zensus J. A., Eckart A., 2012b, A&A, 537, A112
Kelly B. C., Bechtold J., 2007, ApJS, 168, 1
Kidder L. E., 1995, PhRvD, 52, 821
Komossa S., 2006, MmSAI, 77, 733
Komossa S., Burwitz V., Hasinger G., Predehl P., Kaastra J. S., Ikebe Y., 2003, ApJ, 582, L15
Kovács Z., Gergely L., Biermann P. L., 2011, MNRAS, 416, 991
Krichbaum T. P., Britzen S., Standke K. J., Witzel A., Schalinski C. J., Zensus J. A., 1995, PNAS, 92, 11377
Krichbaum T. P., Witzel A., Standke K. J., Graham D. A., Schalinski C. J., Zensus J. A., 1994, in Zensus J. A., Kellermann K. I., eds, Compact Extragalactic Radio Sources MM-VLBI: Bending of Jets in the Vicinity of AGN. p. 39
Kudryavtseva N. A. et al., 2011a, A&A, 526, A51
Kudryavtseva N. A., Gabuzda D. C., Aller M. F., Aller H. D., 2011b, MNRAS, 415, 1631
Kühr H., Witzel A., Pauliny-Toth I. I. K., Nauber U., 1981, A&AS, 45, 367
Lähteenmäki A., Valtaoja E., Wiik K., 1999, ApJ, 511, 112
Lense J., Thirring H., 1918, Phys. Z., 19, 156
Levin J., McWilliams S. T., Contreras H., 2011, CQGra, 28, 175001
Lister M. L. et al., 2013, AJ, 146, 120
Lister M. L. et al., 2009, AJ, 138, 1874
Lister M. L., Smith P. S., 2000, ApJ, 541, 66
Liu Y., Jiang D. R., Gu M. F., 2006, ApJ, 637, 669
Liu Y., Jiang D. R., Shen Z.-Q., Karouzos M., 2010, A&A, 522, A5
Lobanov A. P., Roland J., 2005, A&A, 431, 831
MacFadyen A. I., Milosavljević M., 2008, ApJ, 672, 83
Marscher A. P., Gear W. K., 1985, ApJ, 298, 114
Merritt D., Milosavljević M., 2005, LRR, 8, 8
Murphy D. W., Edwards P. G., 2009, in Hagiwara Y., Fomalont E., Tsuboi M., Yasuhiro M., eds, Approaching Micro-Arcsecond Resolution with VSOP-2: Astrophysics and Technologies Vol. 402 of Astronomical Society of the Pacific Conference Series, VSOP Monitoring Observations of 1928+738. p. 204
Nakamura M., Uchida Y., Hirose S., 2001, NewA, 6, 61
O'Shaughnessy R., Kaplan D. L., Sesana A., Kamble A., 2011, ApJ, 743, 136
Perucho M., Kovalev Y. Y., Lobanov A. P., Hardee P. E., Agudo I., 2012, ApJ, 749, 55
Perucho M., Lobanov A. P., Martí J.-M., Hardee P. E., 2006, A&A, 456, 493
Peters P. C., 1964, PhRv, 136, 1224
Planck Collaboration 2013, preprint (arXiv:1303.5076)
Pushkarev A. B., Kovalev Y. Y., Lister M. L., Savolainen T., 2009, A&A, 507, L33
Pyatunina T. B., Kudryavtseva N. A., Gabuzda D. C., Jorstad S. G., Aller M. F., Aller H. D., Teräsranta H., 2007, MNRAS, 381, 797
Qian S.-J. et al., 2007, ChJAA, 7, 364
Quirrenbach A. et al., 1991, ApJ, 372, L71
Roland J., Britzen S., Kudryavtseva N. A., Witzel A., Karouzos M., 2008, A&A, 483, 125
Roland J., Teyssier R., Roos N., 1994, A&A, 290, 357
Romero G. E., Chajet L., Abraham Z., Fan J. H., 2000, A&A, 360, 57
Roos N., Kaastra J. S., Hummel C. A., 1993, ApJ, 409, 130
Savolainen T., Wiik K., Valtaoja E., Kadler M., Ros E., Tornikoski M., Aller M. F., Aller H. D., 2006, ApJ, 647, 172
Scheuer P. A. G., Readhead A. C. S., 1979, Nature, 277, 182
Schinzel F. K., 2011, PhD Thesis, University of Cologne
Schneider P., 2006, Extragalactic Astronomy and Cosmology, Springer, Berlin
Searle L., Zinn R., 1978, ApJ, 225, 357
Shepherd M. C., 1997, in Hunt G., Payne H., eds, Astronomical Data Analysis Software and Systems VI Vol. 125 of Astronomical Society of the Pacific Conference Series, Difmap: an Interactive Program for Synthesis Imaging. p. 77
Steffen W., 1997, VA, 41, 71
Steffen W., Zensus J. A., Krichbaum T. P., Witzel A., Qian S. J., 1995, A&A, 302, 335
Stirling A. M. et al., 2003, MNRAS, 341, 405
Tanaka T. L., Haiman Z., 2013, CQGra, 30, 22
Thorne K. S., 1974, ApJ, 191, 507
Valtonen M. J., Wiik K., 2012, MNRAS, 421, 1861
Villata M., Raiteri C. M., 1999, A&A, 347, 30
Villata M., Raiteri C. M., Sillanpaa A., Takalo L. O., 1998, MNRAS, 293, L13
Walker R. C., Benson J. M., Unwin S. C., Lystrup M. B., Hunter T. R., Pilbratt G., Hardee P. E., 2001, ApJ, 556, 756
Woo J.-H., Urry C. M., 2002, ApJ, 579, 530

Table 7. Summary of the 15 GHz image parameters. (1) epoch of the VLBA observation, (2) VLBA experiment code, (3)–(4) FWHM minor and major axis of the restoringbeam , respectively, (5) position angle of the major axis of the restoring beam measured from North through East, (6) rms noise of the image, (7) reduced χ^2 of the DIFMAP model-fit, (8) number of the components in the model.

Epoch (1)	VLBA Code (2)	B_{min} [mas] (3)	B_{maj} [mas] (4)	B_{PA} [°] (5)	rms mJy bm^{-1} (6)	Red. χ^2 (7)	Comp. Number (8)
1994 Aug 31	BZ004	0.67	0.76	-67	0.4	1.21	7
1995 Dec 15	BK37A	0.53	0.76	12	0.7	0.39	11
1996 Jan 19	BR034	0.44	1.00	-9	0.6	1.16	11
1996 Mar 22	BR034B	0.46	1.08	-16	0.4	1.01	11
1996 May 16	BK037B	0.52	0.83	-39	0.3	1.39	11
1996 Jul 27	BR034D	0.48	0.97	-16	0.4	2.55	10
1996 Sep 27	BR034E	0.47	0.91	-43	0.4	1.19	8
1996 Oct 27	BK037D	0.42	0.65	22	0.5	0.85	11
1996 Dec 06	BR034F	0.48	1.00	-25	0.5	1.47	8
1997 Aug 28	BK052A	0.54	0.76	-1	0.5	0.47	12
1998 Mar 19	BK052C	0.54	0.85	15	0.5	0.44	11
1998 Aug 03	BT039	0.54	0.71	-8	0.3	1.19	12
1999 Jan 02	BG077D	0.56	0.64	-13	0.5	0.44	12
1999 Jul 17	BP053	0.60	0.70	-49	0.2	1.27	12
1999 Jul 24	BA037	0.64	0.69	56	0.3	1.23	12
1999 Jul 26	BM114B	0.55	1.29	14	0.3	7.56	12
1999 Oct 16	BA037B	0.56	0.64	49	0.3	1.26	12
1999 Dec 23	BA037C	0.55	0.64	59	0.3	1.36	12
2000 Jan 02	BP053B	0.55	0.74	-23	0.1	1.29	12
2000 May 08	BP053C	0.58	0.71	-13	0.1	1.27	12
2001 Mar 04	BK068E	0.53	0.80	-6	0.3	2.58	12
2001 May 17	BT056	0.54	0.74	-12	0.4	1.47	10
2001 Jun 30	BA051A	0.54	0.76	16	0.3	1.25	11
2001 Nov 02	BA051B	0.53	0.75	18	0.3	1.30	11
2001 Dec 22	BR077G	0.53	0.80	-13	0.2	2.45	10
2002 Jan 07	BA051C	0.57	0.81	24	0.3	1.25	9
2002 Feb 18	BR077K	0.55	0.83	5	0.2	3.14	9
2002 Jun 15	BL111B	0.52	0.66	-56	0.3	1.15	10
2003 Aug 28	BL111J	0.61	0.70	40	0.3	1.19	11
2004 Aug 19	BM209B	0.56	1.11	-75	0.3	1.50	10
2005 Mar 23	BL123D	0.59	0.65	-74	0.3	1.24	10
2005 Jul 24	BL123J	0.57	0.69	-35	0.2	1.19	10
2006 Apr 28	BL137D	0.59	0.72	-58	0.4	1.18	10
2007 Mar 02	BL137O	0.65	0.72	-52	0.3	1.13	10
2007 Jul 03	BL149AC	0.64	0.67	39	0.2	1.26	10
2008 Jul 30	BL149AL	0.62	0.65	34	0.2	1.44	10
2009 Jan 07	BL149BG	0.64	0.71	-85	0.2	1.21	10
2009 May 28	BL149BL	0.62	0.66	-69	0.2	1.23	10
2010 Jan 16	BL149CG	0.67	0.77	79	0.2	1.13	10
2010 Sep 29	BL149CR	0.60	0.63	21	0.2	1.29	10
2011 May 26	BL149DI	0.61	0.66	-10	0.2	1.17	11
2012 Jan 14	BL178AF	0.68	0.75	42	0.2	1.06	11
2012 Aug 03	BL178AN	0.65	0.69	53	0.1	1.93	11
2012 Nov 02	BL178AR	0.63	0.68	73	0.2	1.19	12
2013 Jan 21	BL178AY	0.67	0.71	-86	0.2	1.13	12

Table 8: Circular Gaussian model-fit results for S5 1928+738. (1) epoch of observation, (2) flux density, (3)–(4) position of the component center with respect to the core, (5) FWHM, (6) jet-component identification.

Epoch [yr]	Flux density [Jy]	x [mas]	y [mas]	d [mas]	CO
1994.67	0.606 ± 0.044	0.000 ± 0.040	0.000 ± 0.037	0.145 ± 0.003	CS
	0.462 ± 0.045	0.227 ± 0.040	-0.311 ± 0.037	0.144 ± 0.005	Cg
	0.407 ± 0.042	0.561 ± 0.048	-1.238 ± 0.045	0.301 ± 0.007	C7
	0.408 ± 0.042	0.258 ± 0.051	-1.613 ± 0.049	0.350 ± 0.007	C6
	0.078 ± 0.020	1.153 ± 0.087	-3.282 ± 0.086	0.789 ± 0.064	C3
	0.038 ± 0.022	2.203 ± 0.206	-7.417 ± 0.206	2.029 ± 0.580	C2
	0.035 ± 0.012	2.675 ± 0.142	-10.212 ± 0.141	1.366 ± 0.175	C1
1995.96	0.631 ± 0.039	0.000 ± 0.027	0.000 ± 0.037	0.020 ± 0.002	CS
	0.402 ± 0.031	0.086 ± 0.027	-0.213 ± 0.037	0.038 ± 0.003	Cg
	0.781 ± 0.046	0.348 ± 0.028	-0.609 ± 0.038	0.063 ± 0.002	C8
	0.151 ± 0.020	0.359 ± 0.031	-0.848 ± 0.040	0.146 ± 0.008	B1
	0.416 ± 0.043	0.715 ± 0.036	-1.616 ± 0.044	0.236 ± 0.005	C7
	0.233 ± 0.032	0.246 ± 0.043	-1.928 ± 0.050	0.330 ± 0.010	C6
	0.224 ± 0.032	0.366 ± 0.042	-2.195 ± 0.049	0.324 ± 0.011	C5
	0.049 ± 0.012	1.271 ± 0.063	-3.345 ± 0.067	0.564 ± 0.043	C4
	0.025 ± 0.009	1.314 ± 0.071	-4.222 ± 0.075	0.654 ± 0.085	C3
	0.020 ± 0.008	2.768 ± 0.082	-8.220 ± 0.086	0.779 ± 0.130	C2
	0.052 ± 0.022	2.932 ± 0.215	-10.709 ± 0.216	2.128 ± 0.352	C1
1996.05	0.160 ± 0.035	0.000 ± 0.023	0.000 ± 0.048	0.067 ± 0.033	CS
	0.971 ± 0.086	0.169 ± 0.023	-0.335 ± 0.048	0.046 ± 0.006	Cg
	0.741 ± 0.074	0.457 ± 0.023	-0.832 ± 0.048	0.043 ± 0.007	C8
	0.225 ± 0.041	0.518 ± 0.031	-1.027 ± 0.052	0.209 ± 0.025	B2
	0.417 ± 0.045	0.820 ± 0.037	-1.866 ± 0.056	0.294 ± 0.009	C7
	0.289 ± 0.037	0.357 ± 0.038	-2.176 ± 0.057	0.306 ± 0.013	C6
	0.129 ± 0.025	0.551 ± 0.033	-2.600 ± 0.054	0.248 ± 0.028	C5
	0.024 ± 0.010	1.463 ± 0.041	-3.513 ± 0.059	0.342 ± 0.128	C4
	0.050 ± 0.014	1.293 ± 0.085	-4.291 ± 0.094	0.815 ± 0.087	C3
	0.029 ± 0.020	1.940 ± 0.178	-8.667 ± 0.183	1.769 ± 0.694	C2
	0.051 ± 0.019	3.369 ± 0.182	-10.768 ± 0.187	1.811 ± 0.265	C1
1996.22	0.362 ± 0.058	0.000 ± 0.025	0.000 ± 0.047	0.073 ± 0.021	CS
	0.810 ± 0.086	0.115 ± 0.025	-0.254 ± 0.047	0.060 ± 0.009	Cg
	0.713 ± 0.057	0.384 ± 0.026	-0.698 ± 0.048	0.097 ± 0.005	C8
	0.293 ± 0.037	0.465 ± 0.030	-0.964 ± 0.050	0.178 ± 0.013	B3
	0.387 ± 0.038	0.773 ± 0.037	-1.816 ± 0.055	0.284 ± 0.008	C7
	0.249 ± 0.034	0.282 ± 0.039	-2.048 ± 0.056	0.304 ± 0.016	C6
	0.182 ± 0.029	0.451 ± 0.038	-2.480 ± 0.055	0.290 ± 0.022	C5
	0.053 ± 0.017	1.353 ± 0.073	-3.471 ± 0.083	0.687 ± 0.101	C4
	0.026 ± 0.015	1.454 ± 0.069	-4.622 ± 0.080	0.644 ± 0.292	C3
	0.059 ± 0.040	2.515 ± 0.188	-9.207 ± 0.192	1.861 ± 0.722	C2
	0.031 ± 0.026	2.920 ± 0.117	-11.484 ± 0.124	1.144 ± 0.740	C1
1996.38	0.565 ± 0.044	0.000 ± 0.030	0.000 ± 0.033	0.050 ± 0.003	CS
	0.872 ± 0.055	0.091 ± 0.031	-0.192 ± 0.033	0.060 ± 0.002	Cg
	0.822 ± 0.053	0.365 ± 0.031	-0.646 ± 0.034	0.093 ± 0.002	C8
	0.268 ± 0.030	0.406 ± 0.034	-0.874 ± 0.036	0.153 ± 0.007	B4
	0.457 ± 0.042	0.740 ± 0.043	-1.734 ± 0.045	0.309 ± 0.005	C7
	0.264 ± 0.032	0.247 ± 0.042	-2.058 ± 0.044	0.299 ± 0.009	C6
	0.205 ± 0.028	0.449 ± 0.049	-2.380 ± 0.051	0.385 ± 0.012	C5
	0.069 ± 0.015	1.278 ± 0.077	-3.505 ± 0.078	0.710 ± 0.043	C4
	0.028 ± 0.010	1.434 ± 0.077	-4.665 ± 0.078	0.710 ± 0.106	C3
	0.067 ± 0.022	2.643 ± 0.179	-8.760 ± 0.179	1.760 ± 0.184	C2
	0.051 ± 0.017	2.953 ± 0.159	-11.306 ± 0.160	1.566 ± 0.170	C1
1996.57	1.101 ± 0.086	0.000 ± 0.025	0.000 ± 0.044	0.047 ± 0.004	CS
	0.269 ± 0.043	0.163 ± 0.025	-0.275 ± 0.044	0.021 ± 0.017	Cg
	0.913 ± 0.063	0.349 ± 0.028	-0.633 ± 0.046	0.133 ± 0.003	C8
	0.126 ± 0.035	0.481 ± 0.029	-1.080 ± 0.031	0.061 ± 0.045	B5
	0.429 ± 0.044	0.711 ± 0.040	-1.694 ± 0.054	0.312 ± 0.008	C7
	0.263 ± 0.034	0.213 ± 0.040	-2.049 ± 0.054	0.312 ± 0.013	C6

Table 8 – *Continued from previous page*

	0.116 ± 0.023	0.442 ± 0.029	-2.385 ± 0.046	0.150 ± 0.027	C5
	0.065 ± 0.017	1.257 ± 0.073	-3.410 ± 0.082	0.690 ± 0.062	C4
	0.013 ± 0.008	1.438 ± 0.054	-4.553 ± 0.065	0.485 ± 0.245	C3
	0.037 ± 0.014	2.601 ± 0.144	-8.850 ± 0.148	1.419 ± 0.219	C2
	0.021 ± 0.010	2.917 ± 0.129	-11.161 ± 0.134	1.263 ± 0.312	C1
1996.74	0.548 ± 0.072	0.000 ± 0.029	0.000 ± 0.030	0.048 ± 0.010	CS
	1.056 ± 0.070	0.135 ± 0.030	-0.291 ± 0.031	0.095 ± 0.003	Cg
	0.838 ± 0.089	0.427 ± 0.031	-0.776 ± 0.032	0.113 ± 0.007	C8
	0.354 ± 0.046	0.791 ± 0.039	-1.881 ± 0.040	0.266 ± 0.011	C7
	0.338 ± 0.045	0.360 ± 0.044	-2.334 ± 0.045	0.338 ± 0.012	C6
	0.106 ± 0.033	1.146 ± 0.137	-3.585 ± 0.138	1.343 ± 0.147	C4
	0.065 ± 0.023	2.754 ± 0.169	-9.167 ± 0.169	1.664 ± 0.211	C2
	0.027 ± 0.015	2.842 ± 0.154	-12.307 ± 0.154	1.510 ± 0.414	C1
1996.82	0.482 ± 0.076	0.000 ± 0.022	0.000 ± 0.030	0.028 ± 0.003	CS
	0.921 ± 0.062	0.077 ± 0.023	-0.246 ± 0.031	0.070 ± 0.001	Cg
	0.532 ± 0.024	0.353 ± 0.028	-0.650 ± 0.034	0.170 ± 0.009	C8
	0.539 ± 0.025	0.422 ± 0.024	-0.864 ± 0.032	0.101 ± 0.008	B6
	0.323 ± 0.036	0.792 ± 0.031	-1.929 ± 0.037	0.221 ± 0.013	C7
	0.149 ± 0.017	0.235 ± 0.034	-2.224 ± 0.040	0.258 ± 0.002	C6
	0.231 ± 0.022	0.456 ± 0.043	-2.479 ± 0.047	0.368 ± 0.001	C5
	0.041 ± 0.008	1.391 ± 0.050	-3.581 ± 0.054	0.445 ± 0.003	C4
	0.025 ± 0.007	1.470 ± 0.088	-4.488 ± 0.090	0.849 ± 0.040	C3
	0.025 ± 0.007	2.730 ± 0.088	-8.647 ± 0.090	0.849 ± 0.041	C2
	0.032 ± 0.018	3.183 ± 0.202	-10.713 ± 0.203	2.004 ± 0.493	C1
1996.93	1.080 ± 0.073	0.000 ± 0.026	0.000 ± 0.040	0.038 ± 0.003	CS
	0.346 ± 0.034	0.193 ± 0.027	-0.354 ± 0.040	0.061 ± 0.007	Cg
	0.882 ± 0.035	0.372 ± 0.027	-0.698 ± 0.041	0.095 ± 0.001	C8
	0.339 ± 0.029	0.738 ± 0.037	-1.743 ± 0.048	0.263 ± 0.006	C7
	0.373 ± 0.047	0.320 ± 0.051	-2.232 ± 0.060	0.444 ± 0.014	C5
	0.039 ± 0.011	1.371 ± 0.040	-3.645 ± 0.050	0.306 ± 0.063	C4
	0.033 ± 0.007	1.734 ± 0.169	-5.693 ± 0.172	1.674 ± 0.785	C3
	0.055 ± 0.024	2.764 ± 0.151	-11.212 ± 0.154	1.484 ± 0.294	C1
1997.66	0.445 ± 0.059	0.000 ± 0.027	0.000 ± 0.038	0.035 ± 0.001	CS
	0.915 ± 0.063	0.058 ± 0.027	-0.219 ± 0.038	0.039 ± 0.001	Cg
	0.229 ± 0.006	0.322 ± 0.032	-0.629 ± 0.042	0.172 ± 0.012	C9
	0.761 ± 0.014	0.466 ± 0.029	-0.896 ± 0.039	0.111 ± 0.009	C8
	0.220 ± 0.018	0.829 ± 0.045	-2.114 ± 0.052	0.355 ± 0.001	C7
	0.104 ± 0.014	0.266 ± 0.046	-2.386 ± 0.053	0.367 ± 0.002	C6
	0.213 ± 0.017	0.489 ± 0.052	-2.734 ± 0.058	0.442 ± 0.001	C5
	0.048 ± 0.010	1.353 ± 0.070	-3.746 ± 0.075	0.643 ± 0.014	C4
	0.032 ± 0.008	1.468 ± 0.117	-5.075 ± 0.120	1.139 ± 0.062	C3
	0.035 ± 0.007	2.653 ± 0.122	-9.278 ± 0.125	1.194 ± 0.043	C2
	0.052 ± 0.015	2.983 ± 0.168	-11.270 ± 0.170	1.659 ± 0.126	C1
1998.21	0.635 ± 0.045	0.000 ± 0.028	0.000 ± 0.041	0.072 ± 0.003	CS
	1.071 ± 0.058	0.054 ± 0.031	-0.239 ± 0.043	0.149 ± 0.002	Cg
	0.367 ± 0.036	0.444 ± 0.036	-0.812 ± 0.047	0.228 ± 0.006	C9
	0.645 ± 0.047	0.492 ± 0.035	-1.088 ± 0.046	0.212 ± 0.003	C8
	0.144 ± 0.019	0.860 ± 0.054	-2.214 ± 0.062	0.465 ± 0.012	C7
	0.236 ± 0.024	0.465 ± 0.066	-2.618 ± 0.072	0.599 ± 0.009	C6
	0.058 ± 0.012	0.528 ± 0.046	-3.198 ± 0.055	0.366 ± 0.027	C5
	0.049 ± 0.011	1.384 ± 0.075	-3.908 ± 0.081	0.703 ± 0.048	C4
	0.021 ± 0.008	1.620 ± 0.081	-5.565 ± 0.087	0.767 ± 0.123	C3
	0.047 ± 0.019	2.687 ± 0.181	-9.720 ± 0.184	1.793 ± 0.273	C2
	0.044 ± 0.022	2.743 ± 0.225	-12.199 ± 0.227	2.232 ± 0.492	C1
1998.59	0.737 ± 0.046	0.000 ± 0.029	0.000 ± 0.036	0.088 ± 0.002	CS
	0.923 ± 0.052	0.085 ± 0.028	-0.261 ± 0.036	0.057 ± 0.001	Cg
	0.216 ± 0.025	0.262 ± 0.034	-0.586 ± 0.041	0.205 ± 0.006	C10
	0.424 ± 0.035	0.510 ± 0.030	-0.937 ± 0.038	0.134 ± 0.003	C9
	0.481 ± 0.037	0.547 ± 0.039	-1.204 ± 0.045	0.275 ± 0.003	C8
	0.118 ± 0.016	0.938 ± 0.049	-2.276 ± 0.054	0.410 ± 0.010	C7

Table 8 – *Continued from previous page*

	0.245 ± 0.024	0.496 ± 0.066	-2.660 ± 0.070	0.601 ± 0.006	C6
	0.084 ± 0.014	0.573 ± 0.049	-3.287 ± 0.054	0.410 ± 0.014	C5
	0.044 ± 0.010	1.385 ± 0.066	-3.780 ± 0.070	0.606 ± 0.036	C4
	0.039 ± 0.012	1.554 ± 0.123	-5.336 ± 0.125	1.204 ± 0.123	C3
	0.042 ± 0.013	2.642 ± 0.151	-9.580 ± 0.152	1.483 ± 0.150	C2
	0.049 ± 0.017	2.893 ± 0.193	-11.840 ± 0.194	1.908 ± 0.229	C1
1999.01	0.588 ± 0.041	0.000 ± 0.030	0.000 ± 0.034	0.110 ± 0.002	CS
	0.675 ± 0.044	0.050 ± 0.029	-0.185 ± 0.032	0.060 ± 0.001	Cg
	0.322 ± 0.030	0.166 ± 0.035	-0.469 ± 0.038	0.209 ± 0.003	C10
	0.228 ± 0.026	0.501 ± 0.035	-0.887 ± 0.037	0.200 ± 0.005	C9
	0.435 ± 0.035	0.575 ± 0.042	-1.239 ± 0.044	0.308 ± 0.003	C8
	0.098 ± 0.017	0.966 ± 0.058	-2.339 ± 0.060	0.509 ± 0.016	C7
	0.185 ± 0.023	0.478 ± 0.073	-2.749 ± 0.075	0.675 ± 0.011	C6
	0.054 ± 0.013	0.575 ± 0.040	-3.394 ± 0.043	0.284 ± 0.021	C5
	0.065 ± 0.015	1.228 ± 0.104	-3.775 ± 0.105	0.998 ± 0.055	C4
	0.022 ± 0.007	1.644 ± 0.074	-5.766 ± 0.075	0.681 ± 0.068	C3
	0.034 ± 0.012	2.800 ± 0.135	-9.789 ± 0.135	1.315 ± 0.149	C2
	0.038 ± 0.015	2.714 ± 0.176	-11.921 ± 0.176	1.733 ± 0.249	C1
1999.54	0.606 ± 0.036	0.000 ± 0.033	0.000 ± 0.033	0.065 ± 0.002	CS
	1.061 ± 0.048	0.066 ± 0.033	-0.216 ± 0.032	0.040 ± 0.001	Cg
	0.467 ± 0.032	0.226 ± 0.036	-0.578 ± 0.036	0.155 ± 0.002	C10
	0.162 ± 0.019	0.564 ± 0.034	-0.981 ± 0.034	0.109 ± 0.006	C9
	0.435 ± 0.031	0.623 ± 0.046	-1.363 ± 0.046	0.327 ± 0.003	C8
	0.118 ± 0.016	1.029 ± 0.053	-2.529 ± 0.052	0.411 ± 0.011	C7
	0.130 ± 0.017	0.461 ± 0.065	-2.847 ± 0.065	0.563 ± 0.012	C6
	0.095 ± 0.015	0.551 ± 0.051	-3.524 ± 0.050	0.386 ± 0.013	C5
	0.073 ± 0.014	1.243 ± 0.095	-3.937 ± 0.095	0.895 ± 0.036	C4
	0.030 ± 0.007	1.647 ± 0.120	-5.831 ± 0.119	1.150 ± 0.069	C3
	0.041 ± 0.010	2.722 ± 0.157	-9.961 ± 0.157	1.537 ± 0.090	C2
	0.046 ± 0.011	2.689 ± 0.167	-11.746 ± 0.167	1.637 ± 0.092	C1
1999.56	0.525 ± 0.044	0.000 ± 0.034	0.000 ± 0.033	0.050 ± 0.003	CS
	1.123 ± 0.064	0.064 ± 0.034	-0.220 ± 0.033	0.061 ± 0.002	Cg
	0.474 ± 0.042	0.221 ± 0.037	-0.585 ± 0.036	0.157 ± 0.004	C10
	0.177 ± 0.026	0.554 ± 0.038	-0.996 ± 0.038	0.186 ± 0.010	C9
	0.431 ± 0.040	0.626 ± 0.046	-1.385 ± 0.046	0.318 ± 0.005	C8
	0.106 ± 0.019	1.045 ± 0.050	-2.550 ± 0.049	0.372 ± 0.018	C7
	0.147 ± 0.023	0.495 ± 0.069	-2.874 ± 0.069	0.607 ± 0.017	C6
	0.092 ± 0.018	0.544 ± 0.053	-3.575 ± 0.052	0.409 ± 0.021	C5
	0.069 ± 0.017	1.294 ± 0.098	-4.013 ± 0.098	0.920 ± 0.060	C4
	0.023 ± 0.006	1.728 ± 0.082	-6.048 ± 0.081	0.743 ± 0.061	C3
	0.049 ± 0.013	2.876 ± 0.167	-10.111 ± 0.167	1.640 ± 0.113	C2
	0.043 ± 0.013	2.705 ± 0.189	-11.944 ± 0.189	1.861 ± 0.173	C1
1999.57	0.614 ± 0.063	0.000 ± 0.029	0.000 ± 0.058	0.040 ± 0.012	CS
	1.006 ± 0.102	0.062 ± 0.029	-0.209 ± 0.058	0.048 ± 0.012	Cg
	0.525 ± 0.075	0.219 ± 0.034	-0.544 ± 0.061	0.187 ± 0.024	C10
	0.265 ± 0.045	0.559 ± 0.041	-1.075 ± 0.065	0.299 ± 0.035	C9
	0.340 ± 0.051	0.630 ± 0.040	-1.423 ± 0.064	0.280 ± 0.027	C8
	0.114 ± 0.020	1.011 ± 0.038	-2.607 ± 0.063	0.254 ± 0.035	C7
	0.109 ± 0.026	0.434 ± 0.045	-2.852 ± 0.067	0.344 ± 0.066	C6
	0.112 ± 0.026	0.581 ± 0.050	-3.531 ± 0.071	0.416 ± 0.067	C5
	0.050 ± 0.019	1.231 ± 0.070	-4.067 ± 0.086	0.641 ± 0.175	C4
	0.037 ± 0.016	1.596 ± 0.089	-5.517 ± 0.103	0.849 ± 0.244	C3
	0.010 ± 0.007	2.959 ± 0.055	-9.485 ± 0.075	0.476 ± 0.449	C2
	0.065 ± 0.024	2.767 ± 0.192	-11.447 ± 0.199	1.903 ± 0.280	C1
1999.79	0.441 ± 0.039	0.000 ± 0.030	0.000 ± 0.030	0.056 ± 0.003	CS
	0.848 ± 0.055	0.063 ± 0.031	-0.228 ± 0.031	0.086 ± 0.001	Cg
	0.605 ± 0.046	0.225 ± 0.036	-0.593 ± 0.036	0.209 ± 0.002	C10
	0.171 ± 0.024	0.584 ± 0.045	-1.063 ± 0.044	0.331 ± 0.009	C9
	0.353 ± 0.035	0.636 ± 0.045	-1.459 ± 0.044	0.332 ± 0.004	C8
	0.100 ± 0.017	1.067 ± 0.039	-2.636 ± 0.038	0.248 ± 0.011	C7
	0.124 ± 0.019	0.501 ± 0.065	-2.913 ± 0.064	0.572 ± 0.013	C6

Table 8 – *Continued from previous page*

	0.105 ± 0.017	0.571 ± 0.062	-3.623 ± 0.061	0.539 ± 0.015	C5
	0.064 ± 0.014	1.355 ± 0.091	-4.131 ± 0.091	0.857 ± 0.042	C4
	0.022 ± 0.008	1.435 ± 0.056	-6.607 ± 0.056	0.474 ± 0.064	C3
	0.025 ± 0.009	2.546 ± 0.085	-9.594 ± 0.085	0.793 ± 0.096	C2
	0.051 ± 0.013	2.728 ± 0.142	-11.215 ± 0.142	1.390 ± 0.097	C1
1999.98	0.373 ± 0.056	0.000 ± 0.031	0.000 ± 0.029	0.052 ± 0.008	CS
	0.997 ± 0.091	0.059 ± 0.031	-0.251 ± 0.029	0.057 ± 0.003	Cg
	0.698 ± 0.076	0.235 ± 0.036	-0.649 ± 0.035	0.196 ± 0.004	C10
	0.175 ± 0.028	0.615 ± 0.044	-1.193 ± 0.043	0.318 ± 0.010	C9
	0.287 ± 0.036	0.656 ± 0.042	-1.572 ± 0.041	0.292 ± 0.006	C8
	0.134 ± 0.024	1.082 ± 0.043	-2.699 ± 0.041	0.297 ± 0.013	C7
	0.143 ± 0.026	0.477 ± 0.080	-3.088 ± 0.079	0.740 ± 0.025	C6
	0.058 ± 0.016	0.509 ± 0.051	-3.764 ± 0.050	0.406 ± 0.035	C5
	0.075 ± 0.020	1.158 ± 0.097	-3.998 ± 0.097	0.922 ± 0.065	C4
	0.014 ± 0.009	1.539 ± 0.063	-6.354 ± 0.062	0.554 ± 0.184	C3
	0.022 ± 0.010	3.111 ± 0.132	-9.531 ± 0.132	1.284 ± 0.256	C2
	0.048 ± 0.015	2.783 ± 0.141	-11.243 ± 0.141	1.377 ± 0.136	C1
2000.01	0.493 ± 0.045	0.000 ± 0.029	0.000 ± 0.035	0.043 ± 0.004	CS
	0.814 ± 0.057	0.064 ± 0.029	-0.233 ± 0.035	0.056 ± 0.002	Cg
	0.624 ± 0.054	0.238 ± 0.032	-0.622 ± 0.038	0.151 ± 0.003	C10
	0.135 ± 0.025	0.613 ± 0.035	-1.118 ± 0.040	0.205 ± 0.016	C9
	0.312 ± 0.038	0.658 ± 0.044	-1.510 ± 0.049	0.343 ± 0.008	C8
	0.126 ± 0.017	1.084 ± 0.038	-2.654 ± 0.043	0.258 ± 0.008	C7
	0.115 ± 0.016	0.507 ± 0.070	-3.035 ± 0.073	0.642 ± 0.015	C6
	0.076 ± 0.013	0.545 ± 0.047	-3.691 ± 0.052	0.380 ± 0.016	C5
	0.065 ± 0.013	1.206 ± 0.093	-4.131 ± 0.095	0.883 ± 0.039	C4
	0.021 ± 0.006	1.680 ± 0.109	-5.977 ± 0.111	1.051 ± 0.095	C3
	0.032 ± 0.009	2.858 ± 0.160	-10.245 ± 0.161	1.572 ± 0.117	C2
	0.038 ± 0.009	2.627 ± 0.156	-11.892 ± 0.158	1.537 ± 0.094	C1
2000.35	0.474 ± 0.043	0.000 ± 0.029	0.000 ± 0.035	0.019 ± 0.003	CS
	0.790 ± 0.055	0.103 ± 0.030	-0.281 ± 0.036	0.074 ± 0.002	Cg
	0.751 ± 0.076	0.265 ± 0.032	-0.672 ± 0.037	0.135 ± 0.005	C10
	0.145 ± 0.034	0.464 ± 0.034	-0.941 ± 0.039	0.169 ± 0.024	C9
	0.385 ± 0.027	0.706 ± 0.049	-1.573 ± 0.052	0.388 ± 0.003	C8
	0.176 ± 0.037	1.114 ± 0.041	-2.796 ± 0.045	0.290 ± 0.022	C7
	0.147 ± 0.035	0.541 ± 0.069	-3.268 ± 0.072	0.630 ± 0.040	C6
	0.062 ± 0.023	0.609 ± 0.043	-3.943 ± 0.047	0.312 ± 0.063	C5
	0.073 ± 0.027	1.240 ± 0.092	-4.310 ± 0.094	0.870 ± 0.119	C4
	0.022 ± 0.016	1.698 ± 0.095	-6.192 ± 0.097	0.905 ± 0.419	C3
	0.029 ± 0.008	2.928 ± 0.142	-10.247 ± 0.144	1.393 ± 0.097	C2
	0.052 ± 0.011	2.702 ± 0.168	-11.987 ± 0.170	1.659 ± 0.079	C1
2001.17	0.344 ± 0.037	0.000 ± 0.028	0.000 ± 0.040	0.070 ± 0.006	CS
	0.740 ± 0.054	0.055 ± 0.028	-0.179 ± 0.040	0.067 ± 0.003	Cg
	0.367 ± 0.038	0.254 ± 0.030	-0.657 ± 0.042	0.133 ± 0.005	C11
	0.592 ± 0.048	0.409 ± 0.032	-0.929 ± 0.043	0.177 ± 0.003	C10
	0.250 ± 0.030	0.796 ± 0.052	-1.820 ± 0.060	0.447 ± 0.009	C8
	0.127 ± 0.022	1.134 ± 0.046	-3.053 ± 0.055	0.377 ± 0.017	C7
	0.103 ± 0.018	0.581 ± 0.065	-3.683 ± 0.072	0.597 ± 0.022	C6
	0.035 ± 0.009	0.789 ± 0.038	-4.387 ± 0.048	0.268 ± 0.034	C5
	0.054 ± 0.012	1.314 ± 0.099	-4.633 ± 0.103	0.954 ± 0.055	C4
	0.015 ± 0.007	1.614 ± 0.084	-6.500 ± 0.089	0.796 ± 0.180	C3
	0.019 ± 0.007	2.780 ± 0.144	-11.019 ± 0.147	1.415 ± 0.367	C2
	0.040 ± 0.013	2.533 ± 0.128	-12.324 ± 0.131	1.248 ± 0.136	C1
2001.38	0.634 ± 0.044	0.000 ± 0.027	0.000 ± 0.036	0.021 ± 0.002	CS
	0.721 ± 0.047	0.066 ± 0.028	-0.192 ± 0.037	0.073 ± 0.002	Cg
	0.498 ± 0.039	0.275 ± 0.032	-0.688 ± 0.040	0.163 ± 0.003	C11
	0.554 ± 0.041	0.426 ± 0.033	-0.953 ± 0.041	0.181 ± 0.003	C10
	0.281 ± 0.031	0.800 ± 0.057	-1.846 ± 0.062	0.506 ± 0.008	C8
	0.136 ± 0.029	1.123 ± 0.051	-3.088 ± 0.057	0.434 ± 0.025	C7
	0.152 ± 0.024	0.618 ± 0.081	-3.872 ± 0.085	0.765 ± 0.021	C6
	0.069 ± 0.015	1.261 ± 0.082	-4.760 ± 0.086	0.777 ± 0.039	C4

Table 8 – *Continued from previous page*

	0.019 ± 0.009	1.943 ± 0.101	-6.630 ± 0.104	0.970 ± 0.196	C3
	0.083 ± 0.031	2.726 ± 0.215	-11.953 ± 0.216	2.128 ± 0.288	C1
2001.50	0.703 ± 0.047	0.000 ± 0.028	0.000 ± 0.037	0.040 ± 0.002	CS
	0.708 ± 0.047	0.061 ± 0.028	-0.177 ± 0.037	0.060 ± 0.002	Cg
	0.470 ± 0.053	0.279 ± 0.033	-0.686 ± 0.041	0.180 ± 0.006	C11
	0.545 ± 0.057	0.425 ± 0.033	-0.949 ± 0.040	0.174 ± 0.005	C10
	0.276 ± 0.032	0.800 ± 0.058	-1.850 ± 0.063	0.515 ± 0.009	C8
	0.119 ± 0.024	1.126 ± 0.047	-3.072 ± 0.053	0.381 ± 0.022	C7
	0.127 ± 0.023	0.599 ± 0.079	-3.742 ± 0.082	0.738 ± 0.027	C6
	0.105 ± 0.025	1.122 ± 0.102	-4.575 ± 0.105	0.980 ± 0.060	C4
	0.015 ± 0.007	1.772 ± 0.061	-6.451 ± 0.066	0.549 ± 0.117	C3
	0.016 ± 0.007	3.042 ± 0.113	-10.374 ± 0.116	1.100 ± 0.198	C2
	0.059 ± 0.015	2.687 ± 0.154	-12.243 ± 0.156	1.517 ± 0.101	C1
2001.84	0.618 ± 0.052	0.000 ± 0.028	0.000 ± 0.036	0.065 ± 0.003	CS
	1.102 ± 0.069	0.051 ± 0.027	-0.163 ± 0.036	0.051 ± 0.002	Cg
	0.423 ± 0.052	0.282 ± 0.030	-0.681 ± 0.038	0.140 ± 0.007	C11
	0.560 ± 0.060	0.432 ± 0.033	-0.996 ± 0.041	0.197 ± 0.005	C10
	0.242 ± 0.031	0.830 ± 0.061	-1.939 ± 0.066	0.550 ± 0.011	C8
	0.123 ± 0.022	1.080 ± 0.056	-3.215 ± 0.061	0.488 ± 0.020	C7
	0.113 ± 0.022	0.617 ± 0.082	-3.979 ± 0.085	0.772 ± 0.033	C6
	0.080 ± 0.020	1.269 ± 0.101	-4.797 ± 0.104	0.974 ± 0.064	C4
	0.009 ± 0.008	1.869 ± 0.096	-6.464 ± 0.098	0.917 ± 0.544	C3
	0.015 ± 0.007	2.778 ± 0.117	-10.696 ± 0.120	1.143 ± 0.263	C2
	0.057 ± 0.016	2.722 ± 0.149	-12.302 ± 0.151	1.463 ± 0.113	C1
2001.97	0.636 ± 0.040	0.000 ± 0.027	0.000 ± 0.039	0.020 ± 0.002	CS
	1.033 ± 0.051	0.051 ± 0.027	-0.166 ± 0.039	0.054 ± 0.001	Cg
	0.380 ± 0.044	0.279 ± 0.030	-0.697 ± 0.041	0.126 ± 0.007	C11
	0.483 ± 0.050	0.443 ± 0.034	-1.023 ± 0.044	0.210 ± 0.006	C10
	0.207 ± 0.034	0.841 ± 0.061	-1.999 ± 0.067	0.545 ± 0.019	C8
	0.103 ± 0.018	1.078 ± 0.059	-3.203 ± 0.066	0.529 ± 0.021	C7
	0.124 ± 0.022	0.687 ± 0.087	-4.083 ± 0.091	0.824 ± 0.030	C6
	0.050 ± 0.013	1.447 ± 0.080	-4.996 ± 0.085	0.754 ± 0.059	C4
	0.009 ± 0.007	1.616 ± 0.090	-6.729 ± 0.095	0.863 ± 0.427	C3
	0.061 ± 0.020	2.832 ± 0.185	-12.057 ± 0.187	1.827 ± 0.194	C1
2002.02	0.588 ± 0.051	0.000 ± 0.030	0.000 ± 0.038	0.031 ± 0.004	CS
	1.373 ± 0.078	0.050 ± 0.030	-0.168 ± 0.038	0.013 ± 0.002	Cg
	0.403 ± 0.046	0.291 ± 0.034	-0.694 ± 0.041	0.169 ± 0.007	C11
	0.531 ± 0.053	0.439 ± 0.037	-1.039 ± 0.043	0.215 ± 0.006	C10
	0.231 ± 0.034	0.835 ± 0.064	-1.976 ± 0.068	0.570 ± 0.017	C8
	0.141 ± 0.027	1.037 ± 0.061	-3.280 ± 0.065	0.533 ± 0.027	C7
	0.114 ± 0.024	0.690 ± 0.087	-4.260 ± 0.090	0.815 ± 0.044	C6
	0.062 ± 0.020	1.477 ± 0.096	-4.958 ± 0.099	0.917 ± 0.105	C4
	0.085 ± 0.025	2.682 ± 0.204	-12.245 ± 0.206	2.022 ± 0.180	C1
2002.13	0.560 ± 0.050	0.000 ± 0.027	0.000 ± 0.041	0.011 ± 0.004	CS
	1.403 ± 0.078	0.046 ± 0.028	-0.161 ± 0.041	0.035 ± 0.002	Cg
	0.340 ± 0.039	0.283 ± 0.030	-0.695 ± 0.043	0.112 ± 0.007	C11
	0.476 ± 0.046	0.444 ± 0.034	-1.044 ± 0.046	0.204 ± 0.005	C10
	0.202 ± 0.031	0.849 ± 0.063	-1.992 ± 0.070	0.568 ± 0.018	C8
	0.111 ± 0.023	1.023 ± 0.060	-3.274 ± 0.067	0.529 ± 0.032	C7
	0.132 ± 0.028	0.763 ± 0.100	-4.262 ± 0.105	0.965 ± 0.050	C6
	0.032 ± 0.013	1.588 ± 0.058	-5.306 ± 0.066	0.515 ± 0.109	C4
	0.064 ± 0.028	2.891 ± 0.181	-12.187 ± 0.184	1.791 ± 0.333	C1
2002.45	0.473 ± 0.036	0.000 ± 0.031	0.000 ± 0.028	0.051 ± 0.002	CS
	2.061 ± 0.074	0.066 ± 0.031	-0.205 ± 0.028	0.065 ± 0.000	Cg
	0.271 ± 0.034	0.299 ± 0.032	-0.729 ± 0.029	0.099 ± 0.005	C11
	0.445 ± 0.032	0.456 ± 0.038	-1.100 ± 0.035	0.220 ± 0.002	C10
	0.210 ± 0.030	0.874 ± 0.073	-2.160 ± 0.072	0.665 ± 0.014	C8
	0.124 ± 0.020	0.979 ± 0.065	-3.449 ± 0.063	0.570 ± 0.015	C7
	0.094 ± 0.016	0.720 ± 0.091	-4.378 ± 0.090	0.861 ± 0.025	C6
	0.056 ± 0.014	1.500 ± 0.085	-5.071 ± 0.084	0.792 ± 0.050	C4

Table 8 – *Continued from previous page*

	0.015 ± 0.008	1.786 ± 0.150	-7.156 ± 0.150	1.473 ± 0.365	C3
	0.067 ± 0.020	2.611 ± 0.183	-12.321 ± 0.183	1.808 ± 0.156	C1
2003.66	0.338 ± 0.033	0.000 ± 0.032	0.000 ± 0.033	0.018 ± 0.004	CS
	1.356 ± 0.066	0.078 ± 0.033	-0.274 ± 0.034	0.070 ± 0.001	Cg
	0.960 ± 0.056	0.177 ± 0.035	-0.523 ± 0.036	0.147 ± 0.002	C12
	0.163 ± 0.032	0.374 ± 0.037	-0.888 ± 0.038	0.187 ± 0.018	C11
	0.226 ± 0.038	0.592 ± 0.050	-1.431 ± 0.051	0.388 ± 0.016	C10
	0.132 ± 0.030	0.993 ± 0.076	-2.446 ± 0.077	0.693 ± 0.041	C8
	0.079 ± 0.019	1.054 ± 0.079	-3.478 ± 0.079	0.724 ± 0.044	C7
	0.060 ± 0.014	0.848 ± 0.092	-4.397 ± 0.093	0.867 ± 0.052	C6
	0.060 ± 0.013	1.507 ± 0.113	-5.536 ± 0.113	1.081 ± 0.056	C4
	0.006 ± 0.006	2.217 ± 0.155	-7.593 ± 0.155	1.512 ± 1.079	C3
	0.065 ± 0.020	2.721 ± 0.181	-12.818 ± 0.181	1.785 ± 0.170	C1
2004.63	0.325 ± 0.028	0.000 ± 0.051	0.000 ± 0.029	0.041 ± 0.007	CS
	0.694 ± 0.042	0.072 ± 0.051	-0.294 ± 0.030	0.073 ± 0.003	Cg
	1.189 ± 0.061	0.187 ± 0.053	-0.651 ± 0.032	0.138 ± 0.002	C12
	0.602 ± 0.043	0.322 ± 0.052	-0.857 ± 0.031	0.107 ± 0.005	C11
	0.122 ± 0.023	0.614 ± 0.074	-1.561 ± 0.061	0.533 ± 0.037	C10
	0.057 ± 0.016	1.091 ± 0.079	-2.354 ± 0.067	0.602 ± 0.084	C9
	0.059 ± 0.016	1.082 ± 0.064	-3.033 ± 0.048	0.387 ± 0.068	C8
	0.075 ± 0.013	0.897 ± 0.102	-3.977 ± 0.093	0.888 ± 0.038	C7
	0.057 ± 0.012	1.516 ± 0.112	-5.808 ± 0.104	0.997 ± 0.057	C4
	0.056 ± 0.021	2.724 ± 0.224	-13.534 ± 0.220	2.178 ± 0.319	C1
2005.22	0.315 ± 0.029	0.000 ± 0.032	0.000 ± 0.030	0.029 ± 0.003	CS
	0.584 ± 0.039	0.086 ± 0.035	-0.274 ± 0.033	0.133 ± 0.002	Cg
	1.641 ± 0.068	0.247 ± 0.037	-0.743 ± 0.035	0.181 ± 0.001	C12
	0.527 ± 0.039	0.371 ± 0.034	-0.941 ± 0.032	0.117 ± 0.002	C11
	0.110 ± 0.018	0.682 ± 0.062	-1.587 ± 0.061	0.529 ± 0.016	C10
	0.046 ± 0.012	1.262 ± 0.062	-2.346 ± 0.061	0.529 ± 0.037	C9
	0.103 ± 0.017	1.120 ± 0.064	-3.118 ± 0.063	0.552 ± 0.017	C8
	0.066 ± 0.017	0.869 ± 0.106	-4.220 ± 0.105	1.005 ± 0.065	C7
	0.056 ± 0.014	1.482 ± 0.106	-5.888 ± 0.106	1.014 ± 0.061	C4
	0.040 ± 0.016	2.553 ± 0.181	-13.623 ± 0.181	1.782 ± 0.262	C1
2005.56	0.400 ± 0.031	0.000 ± 0.031	0.000 ± 0.033	0.075 ± 0.002	CS
	0.533 ± 0.035	0.092 ± 0.032	-0.299 ± 0.034	0.110 ± 0.002	Cg
	1.527 ± 0.060	0.275 ± 0.036	-0.800 ± 0.038	0.193 ± 0.001	C12
	0.802 ± 0.043	0.378 ± 0.033	-0.987 ± 0.035	0.136 ± 0.001	C11
	0.086 ± 0.014	0.644 ± 0.052	-1.563 ± 0.053	0.422 ± 0.015	C10
	0.068 ± 0.015	1.228 ± 0.063	-2.332 ± 0.064	0.554 ± 0.029	C9
	0.110 ± 0.019	1.140 ± 0.058	-3.211 ± 0.059	0.494 ± 0.017	C8
	0.067 ± 0.015	0.906 ± 0.111	-4.315 ± 0.112	1.072 ± 0.053	C7
	0.062 ± 0.015	1.585 ± 0.124	-5.965 ± 0.124	1.199 ± 0.070	C4
	0.058 ± 0.019	2.721 ± 0.220	-13.583 ± 0.220	2.179 ± 0.232	C1
2006.32	0.493 ± 0.039	0.000 ± 0.034	0.000 ± 0.032	0.055 ± 0.003	CS
	0.620 ± 0.044	0.076 ± 0.034	-0.220 ± 0.031	0.027 ± 0.002	Cg
	0.315 ± 0.041	0.213 ± 0.038	-0.641 ± 0.036	0.180 ± 0.008	C13
	0.891 ± 0.069	0.370 ± 0.041	-0.980 ± 0.039	0.227 ± 0.003	C12
	0.751 ± 0.064	0.461 ± 0.039	-1.172 ± 0.037	0.198 ± 0.004	C11
	0.086 ± 0.024	1.248 ± 0.092	-2.495 ± 0.091	0.852 ± 0.071	C9
	0.106 ± 0.020	1.174 ± 0.061	-3.389 ± 0.060	0.512 ± 0.022	C8
	0.054 ± 0.016	0.931 ± 0.110	-4.505 ± 0.109	1.049 ± 0.100	C7
	0.052 ± 0.016	1.649 ± 0.134	-6.314 ± 0.133	1.298 ± 0.130	C4
	0.035 ± 0.011	2.680 ± 0.149	-13.720 ± 0.149	1.455 ± 0.156	C1
2007.17	0.719 ± 0.056	0.000 ± 0.036	0.000 ± 0.035	0.092 ± 0.003	CS
	0.549 ± 0.049	0.067 ± 0.035	-0.211 ± 0.034	0.049 ± 0.004	Cg
	0.218 ± 0.031	0.258 ± 0.037	-0.660 ± 0.036	0.125 ± 0.011	C13
	0.667 ± 0.054	0.370 ± 0.040	-1.077 ± 0.039	0.194 ± 0.004	C12
	0.647 ± 0.054	0.552 ± 0.043	-1.278 ± 0.042	0.254 ± 0.004	C11
	0.052 ± 0.015	1.415 ± 0.059	-2.592 ± 0.059	0.481 ± 0.057	C9
	0.128 ± 0.023	1.199 ± 0.068	-3.439 ± 0.067	0.580 ± 0.024	C8

Table 8 – *Continued from previous page*

	0.044 ± 0.011	1.059 ± 0.106	-4.866 ± 0.105	0.999 ± 0.064	C7
	0.037 ± 0.010	1.726 ± 0.112	-6.441 ± 0.112	1.065 ± 0.084	C4
	0.043 ± 0.018	2.626 ± 0.247	-14.197 ± 0.247	2.444 ± 0.400	C1
2007.50	0.783 ± 0.047	0.000 ± 0.033	0.000 ± 0.033	0.052 ± 0.002	CS
	0.587 ± 0.041	0.063 ± 0.034	-0.221 ± 0.034	0.090 ± 0.002	Cg
	0.303 ± 0.035	0.264 ± 0.037	-0.683 ± 0.037	0.172 ± 0.006	C13
	0.651 ± 0.051	0.388 ± 0.041	-1.160 ± 0.041	0.240 ± 0.003	C12
	0.616 ± 0.049	0.592 ± 0.043	-1.380 ± 0.043	0.277 ± 0.003	C11
	0.072 ± 0.018	1.398 ± 0.074	-2.682 ± 0.074	0.661 ± 0.046	C9
	0.120 ± 0.022	1.255 ± 0.061	-3.561 ± 0.062	0.519 ± 0.022	C8
	0.041 ± 0.011	0.995 ± 0.109	-4.667 ± 0.110	1.045 ± 0.082	C7
	0.044 ± 0.013	1.633 ± 0.133	-6.393 ± 0.133	1.285 ± 0.111	C4
	0.039 ± 0.016	2.657 ± 0.241	-14.479 ± 0.241	2.384 ± 0.366	C1
2008.58	0.699 ± 0.051	0.000 ± 0.032	0.000 ± 0.033	0.067 ± 0.002	CS
	0.540 ± 0.044	0.062 ± 0.032	-0.218 ± 0.033	0.068 ± 0.003	Cg
	0.315 ± 0.028	0.252 ± 0.035	-0.703 ± 0.035	0.147 ± 0.003	C14
	0.461 ± 0.065	0.383 ± 0.036	-0.965 ± 0.037	0.182 ± 0.009	C13
	0.707 ± 0.081	0.629 ± 0.052	-1.580 ± 0.052	0.415 ± 0.007	C11
	0.046 ± 0.013	1.455 ± 0.064	-2.837 ± 0.064	0.557 ± 0.047	C9
	0.115 ± 0.020	1.306 ± 0.074	-3.810 ± 0.074	0.668 ± 0.022	C8
	0.029 ± 0.014	1.020 ± 0.108	-5.262 ± 0.108	1.032 ± 0.215	C7
	0.035 ± 0.016	1.717 ± 0.138	-6.687 ± 0.139	1.348 ± 0.270	C4
	0.036 ± 0.019	2.453 ± 0.228	-14.731 ± 0.228	2.262 ± 0.551	C1
2009.02	0.778 ± 0.055	0.000 ± 0.036	0.000 ± 0.033	0.058 ± 0.003	CS
	0.616 ± 0.049	0.047 ± 0.036	-0.191 ± 0.033	0.062 ± 0.003	Cg
	0.333 ± 0.049	0.199 ± 0.041	-0.683 ± 0.038	0.210 ± 0.011	C14
	0.529 ± 0.061	0.405 ± 0.041	-1.011 ± 0.038	0.210 ± 0.007	C13
	0.551 ± 0.063	0.667 ± 0.059	-1.689 ± 0.057	0.469 ± 0.009	C11
	0.036 ± 0.009	1.450 ± 0.056	-2.972 ± 0.054	0.433 ± 0.039	C9
	0.103 ± 0.016	1.274 ± 0.080	-3.902 ± 0.078	0.716 ± 0.020	C8
	0.039 ± 0.015	1.373 ± 0.155	-5.796 ± 0.155	1.513 ± 0.232	C7
	0.013 ± 0.007	1.981 ± 0.111	-7.423 ± 0.110	1.051 ± 0.260	C4
	0.032 ± 0.019	2.707 ± 0.254	-14.860 ± 0.254	2.520 ± 0.751	C1
2009.41	0.906 ± 0.069	0.000 ± 0.034	0.000 ± 0.032	0.075 ± 0.002	CS
	1.186 ± 0.079	0.051 ± 0.033	-0.179 ± 0.032	0.045 ± 0.002	Cg
	0.314 ± 0.041	0.221 ± 0.037	-0.740 ± 0.036	0.178 ± 0.008	C14
	0.583 ± 0.056	0.425 ± 0.040	-1.087 ± 0.038	0.223 ± 0.004	C13
	0.463 ± 0.032	0.733 ± 0.060	-1.800 ± 0.059	0.506 ± 0.003	C11
	0.032 ± 0.008	1.424 ± 0.051	-3.028 ± 0.050	0.387 ± 0.036	C9
	0.105 ± 0.016	1.329 ± 0.084	-3.977 ± 0.084	0.777 ± 0.019	C8
	0.035 ± 0.013	1.203 ± 0.138	-5.820 ± 0.137	1.336 ± 0.181	C7
	0.021 ± 0.011	1.994 ± 0.176	-7.459 ± 0.176	1.728 ± 0.448	C4
	0.032 ± 0.018	2.493 ± 0.243	-15.049 ± 0.243	2.406 ± 0.637	C1
2010.04	0.479 ± 0.038	0.000 ± 0.038	0.000 ± 0.034	0.047 ± 0.004	CS
	2.109 ± 0.076	0.079 ± 0.039	-0.209 ± 0.034	0.063 ± 0.001	Cg
	0.337 ± 0.030	0.126 ± 0.038	-0.389 ± 0.034	0.035 ± 0.005	C15
	0.279 ± 0.031	0.319 ± 0.041	-0.928 ± 0.038	0.164 ± 0.007	C14
	0.391 ± 0.037	0.511 ± 0.048	-1.279 ± 0.045	0.295 ± 0.006	C13
	0.292 ± 0.033	0.889 ± 0.073	-2.064 ± 0.071	0.621 ± 0.011	C11
	0.106 ± 0.018	1.397 ± 0.097	-4.032 ± 0.095	0.893 ± 0.032	C8
	0.029 ± 0.011	1.196 ± 0.127	-6.013 ± 0.126	1.214 ± 0.190	C7
	0.021 ± 0.011	2.142 ± 0.193	-7.874 ± 0.192	1.888 ± 0.487	C4
	0.041 ± 0.035	2.501 ± 0.418	-15.792 ± 0.417	4.159 ± 2.074	C1
2010.74	1.167 ± 0.067	0.000 ± 0.031	0.000 ± 0.032	0.055 ± 0.001	CS
	2.185 ± 0.091	0.097 ± 0.032	-0.180 ± 0.033	0.089 ± 0.001	Cg
	0.213 ± 0.037	0.182 ± 0.035	-0.534 ± 0.036	0.174 ± 0.012	C15
	0.302 ± 0.044	0.398 ± 0.036	-1.016 ± 0.037	0.200 ± 0.009	C14
	0.270 ± 0.042	0.570 ± 0.043	-1.354 ± 0.043	0.297 ± 0.010	C13
	0.214 ± 0.039	1.053 ± 0.080	-2.185 ± 0.080	0.737 ± 0.025	C11
	0.101 ± 0.019	1.400 ± 0.108	-4.068 ± 0.108	1.035 ± 0.036	C8

Table 8 – *Continued from previous page*

	0.023 ± 0.009	1.210 ± 0.108	-5.870 ± 0.108	1.038 ± 0.161	C7
	0.023 ± 0.013	2.226 ± 0.175	-7.882 ± 0.175	1.725 ± 0.474	C4
	0.021 ± 0.013	2.715 ± 0.199	-15.223 ± 0.199	1.967 ± 0.648	C1
2011.40	0.601 ± 0.044	0.000 ± 0.031	0.000 ± 0.033	0.058 ± 0.002	CS
	1.676 ± 0.073	0.090 ± 0.032	-0.210 ± 0.034	0.087 ± 0.001	Cg
	0.649 ± 0.045	0.269 ± 0.031	-0.376 ± 0.033	0.045 ± 0.002	C16
	0.362 ± 0.034	0.191 ± 0.033	-0.640 ± 0.035	0.116 ± 0.004	C15
	0.190 ± 0.022	0.465 ± 0.036	-1.137 ± 0.038	0.187 ± 0.006	C14
	0.238 ± 0.025	0.641 ± 0.043	-1.473 ± 0.045	0.308 ± 0.005	C13
	0.182 ± 0.026	1.152 ± 0.093	-2.372 ± 0.094	0.880 ± 0.019	C11
	0.090 ± 0.019	1.394 ± 0.119	-4.201 ± 0.119	1.146 ± 0.053	C8
	0.029 ± 0.013	1.408 ± 0.158	-6.456 ± 0.159	1.555 ± 0.274	C7
	0.011 ± 0.011	2.548 ± 0.206	-8.944 ± 0.206	2.036 ± 1.275	C4
	0.029 ± 0.026	2.422 ± 0.360	-15.656 ± 0.360	3.586 ± 1.971	C1
2012.04	0.469 ± 0.038	0.000 ± 0.036	0.000 ± 0.036	0.020 ± 0.004	CS
	1.595 ± 0.069	0.079 ± 0.037	-0.177 ± 0.037	0.094 ± 0.001	Cg
	0.980 ± 0.055	0.252 ± 0.038	-0.510 ± 0.038	0.136 ± 0.002	C16
	0.343 ± 0.032	0.263 ± 0.037	-0.802 ± 0.038	0.115 ± 0.005	C15
	0.234 ± 0.029	0.575 ± 0.046	-1.373 ± 0.046	0.286 ± 0.010	C14
	0.084 ± 0.018	0.786 ± 0.047	-1.750 ± 0.048	0.313 ± 0.028	C13
	0.142 ± 0.018	1.309 ± 0.087	-2.678 ± 0.087	0.796 ± 0.015	C11
	0.071 ± 0.020	1.441 ± 0.115	-4.279 ± 0.115	1.093 ± 0.092	C8
	0.024 ± 0.009	1.398 ± 0.162	-6.179 ± 0.163	1.585 ± 0.233	C7
	0.014 ± 0.008	2.310 ± 0.177	-8.538 ± 0.177	1.734 ± 0.487	C4
	0.031 ± 0.035	2.124 ± 0.455	-16.386 ± 0.455	4.534 ± 3.414	C1
2012.59	0.338 ± 0.029	0.000 ± 0.034	0.000 ± 0.034	0.050 ± 0.003	CS
	1.652 ± 0.063	0.106 ± 0.036	-0.199 ± 0.035	0.123 ± 0.001	Cg
	0.771 ± 0.036	0.303 ± 0.038	-0.632 ± 0.037	0.171 ± 0.001	C16
	0.387 ± 0.025	0.309 ± 0.036	-0.886 ± 0.035	0.124 ± 0.002	C15
	0.199 ± 0.028	0.619 ± 0.045	-1.509 ± 0.045	0.303 ± 0.011	C14
	0.078 ± 0.018	0.883 ± 0.062	-1.872 ± 0.062	0.523 ± 0.035	C13
	0.110 ± 0.021	1.515 ± 0.071	-2.864 ± 0.071	0.628 ± 0.029	C11
	0.070 ± 0.020	1.310 ± 0.117	-3.705 ± 0.117	1.119 ± 0.097	C9
	0.041 ± 0.016	1.549 ± 0.125	-4.966 ± 0.125	1.200 ± 0.187	C8
	0.028 ± 0.019	1.811 ± 0.274	-7.896 ± 0.274	2.716 ± 0.959	C4
	0.028 ± 0.034	2.225 ± 0.486	-16.406 ± 0.486	4.844 ± 3.991	C1
2012.84	0.492 ± 0.032	0.000 ± 0.034	0.000 ± 0.032	0.059 ± 0.002	CS
	1.328 ± 0.053	0.087 ± 0.035	-0.177 ± 0.033	0.095 ± 0.001	Cg
	0.606 ± 0.040	0.289 ± 0.037	-0.642 ± 0.035	0.143 ± 0.002	C16
	0.349 ± 0.031	0.323 ± 0.036	-0.904 ± 0.034	0.119 ± 0.004	C15
	0.167 ± 0.022	0.607 ± 0.044	-1.529 ± 0.043	0.288 ± 0.009	C14
	0.066 ± 0.012	0.926 ± 0.069	-1.952 ± 0.068	0.600 ± 0.024	C13
	0.096 ± 0.018	1.521 ± 0.068	-2.890 ± 0.067	0.586 ± 0.023	C11
	0.062 ± 0.015	1.332 ± 0.099	-3.646 ± 0.098	0.929 ± 0.062	C9
	0.038 ± 0.009	1.462 ± 0.109	-4.772 ± 0.109	1.041 ± 0.059	C8
	0.015 ± 0.007	1.382 ± 0.144	-6.553 ± 0.143	1.395 ± 0.264	C7
	0.015 ± 0.008	2.377 ± 0.180	-8.840 ± 0.179	1.765 ± 0.444	C4
	0.028 ± 0.030	2.331 ± 0.455	-16.564 ± 0.455	4.539 ± 3.146	C1
2013.06	0.412 ± 0.029	0.000 ± 0.036	0.000 ± 0.034	0.037 ± 0.003	CS
	1.535 ± 0.056	0.085 ± 0.037	-0.203 ± 0.035	0.098 ± 0.001	Cg
	0.562 ± 0.034	0.300 ± 0.038	-0.700 ± 0.036	0.139 ± 0.002	C16
	0.362 ± 0.027	0.346 ± 0.039	-0.976 ± 0.037	0.168 ± 0.003	C15
	0.153 ± 0.021	0.635 ± 0.043	-1.609 ± 0.041	0.247 ± 0.011	C14
	0.064 ± 0.015	0.948 ± 0.072	-2.069 ± 0.071	0.631 ± 0.041	C13
	0.098 ± 0.018	1.552 ± 0.064	-2.989 ± 0.063	0.538 ± 0.023	C11
	0.074 ± 0.014	1.359 ± 0.097	-3.725 ± 0.097	0.908 ± 0.037	C9
	0.040 ± 0.011	1.499 ± 0.117	-4.905 ± 0.116	1.113 ± 0.093	C8
	0.014 ± 0.006	1.421 ± 0.144	-6.858 ± 0.143	1.395 ± 0.214	C7
	0.014 ± 0.007	2.285 ± 0.147	-8.993 ± 0.146	1.426 ± 0.301	C4
	0.028 ± 0.025	2.251 ± 0.422	-16.326 ± 0.422	4.206 ± 2.293	C1

Table 9. The inclination and position angles of the jet axis obtained from the parametric fit on the 15 GHz data.

Epoch	λ_0	ι_0
1995.96	153.05 ± 6.38	8.20 ± 1.13
1996.05	153.67 ± 4.75	10.14 ± 1.23
1996.22	154.41 ± 5.36	9.26 ± 1.25
1996.38	153.04 ± 6.33	9.04 ± 1.07
1996.57	158.42 ± 7.40	9.70 ± 1.77
1996.74	152.34 ± 6.06	10.08 ± 1.14
1996.82	158.09 ± 4.30	7.17 ± 0.68
1996.93	155.77 ± 5.72	7.57 ± 1.00
1997.66	159.22 ± 3.17	7.31 ± 0.51
1998.21	159.40 ± 6.37	9.01 ± 1.19
1998.59	158.60 ± 3.93	8.02 ± 0.62
1999.01	158.89 ± 6.15	7.64 ± 0.83
1999.54	155.62 ± 6.76	8.72 ± 0.97
1999.56	156.45 ± 6.93	8.73 ± 1.00
1999.57	158.41 ± 4.97	9.20 ± 1.10
1999.79	156.98 ± 7.91	8.88 ± 1.17
1999.98	157.10 ± 8.01	9.63 ± 1.27
2000.01	155.37 ± 6.86	9.46 ± 1.20
2000.35	154.52 ± 6.43	9.07 ± 1.07
2001.17	155.01 ± 7.84	8.72 ± 1.46
2001.38	154.38 ± 7.99	8.56 ± 1.41
2001.50	154.22 ± 8.08	8.44 ± 1.40
2001.84	155.21 ± 8.11	8.32 ± 1.43
2001.97	156.44 ± 7.87	8.63 ± 1.50
2002.02	155.68 ± 8.04	8.59 ± 1.42
2002.13	156.90 ± 7.55	8.63 ± 1.48
2002.45	153.07 ± 5.21	8.68 ± 0.80
2003.66	161.05 ± 4.80	7.30 ± 0.66
2004.63	164.64 ± 7.66	7.85 ± 0.73
2005.22	161.71 ± 6.04	8.79 ± 0.85
2005.56	161.05 ± 5.40	9.35 ± 0.88
2006.32	159.25 ± 6.51	8.07 ± 0.83
2007.17	155.18 ± 6.48	8.45 ± 0.92
2007.50	155.19 ± 6.62	8.76 ± 1.02
2008.58	156.68 ± 6.33	7.95 ± 0.95
2009.02	158.33 ± 7.04	8.03 ± 1.01
2009.41	160.33 ± 6.86	8.52 ± 1.06
2010.04	162.50 ± 5.65	6.70 ± 0.66
2010.74	162.49 ± 5.19	7.86 ± 0.73
2011.40	160.72 ± 4.24	6.86 ± 0.54
2012.04	160.43 ± 4.97	8.52 ± 0.74
2012.59	158.35 ± 5.74	9.25 ± 0.89
2012.84	156.87 ± 7.80	8.70 ± 1.10
2013.06	156.85 ± 7.37	9.43 ± 1.13